A CUBOIDAL OPEN CELL MODEL FOR CONSTITUTIVE MODELING OF SURFACE EFFECTS IN FLUID-SATURATED POROUS MATERIALS

Fei Ti , Xin Chen , Moxiao Li , Shaobao Liu , Tian Jian Lu

PII: S0022-5096(23)00050-9
DOI: https://doi.org/10.1016/j.jmps.2023.105246
Reference: MPS 105246

To appear in: *Journal of the Mechanics and Physics of Solids*

Received date: 12 October 2022
Revised date: 17 January 2023
Accepted date: 9 February 2023

Please cite this article as: Fei Ti , Xin Chen , Moxiao Li , Shaobao Liu , Tian Jian Lu , A CUBOIDAL OPEN CELL MODEL FOR CONSTITUTIVE MODELING OF SURFACE EFFECTS IN FLUID-SATURATED POROUS MATERIALS, *Journal of the Mechanics and Physics of Solids* (2023), doi: https://doi.org/10.1016/j.jmps.2023.105246

A CUBOIDAL OPEN CELL MODEL FOR CONSTITUTIVE MODELING OF SURFACE EFFECTS IN FLUID-SATURATED POROUS MATERIALS

Fei Ti[a,b], Xin Chen[c*], Moxiao Li[a,b], Shaobao Liu[a,b], Tian Jian Lu[a,b*]

[a] *State Key Laboratory of Mechanics and Control of Mechanical Structures, Nanjing University of Aeronautics and Astronautics, Nanjing 210016, P.R. China*
[b] *MIIT Key Laboratory of Multifunctional Lightweight Materials and Structures, Nanjing University of Aeronautics and Astronautics, Nanjing 210016, P.R. China*
[c] *Xi'an Modern Chemistry Research Institute, Xi'an, 710065, P.R. China*
[*] *Corresponding authors: tjlu@nuaa.edu.cn; xinchern@126.com*

Abstract

Fluid-saturated porous elastic materials, made up of connected networks of solid ligaments and characteristically having open pores, are commonly found in geological, biological and engineering materials. Surface effects can affect significantly the mechanical performance of such porous materials at macro scale, especially when the solid ligaments and the pores have micro or nano scale sizes. In the present study, in order to explicitly link pore-level geometrical parameters and surface effects with effective poroelastic properties as well as constitutive equations governing poroelastic deformation, we combine the top-down homogenization approach presented a previous study (Chen et al., 2021) with the bottom-up micromechanics approach. Inspired by the Gibson-Ashby cubic cell model for open-cell foams and the cellular networks typically found in fluid-saturated porous materials, we propose a cuboidal open cell model, with surface effects and fluid compressibility accounted for. For two limiting cases, *i.e.*, the undrained state and the drained state, we demonstrate that both the surface moduli and residual surface stress (*i.e.*, surface tension) prevent the deformation of solid ligaments, thus stiffening the porous material with enlarged effective Young's moduli. Further, we reveal that the two surface effect parameters (*i.e.*, residual surface stress versus surface moduli) exhibit a coupling effect on effective moduli: when one parameter is large enough, the variation of the other affects significantly the effective moduli. As applications of the proposed model, we characterize mechanical behaviors of the porous material under typical loadings (*e.g.*, uniaxial and non-proportional multiaxial tension) in both undrained and drained states; we also describe, for the first time, the stress concentration of a compressible liquid inclusion (*e.g.*, a cell) with surface tension embedded in a fluid-saturated porous material with surface effects. Results of this study are beneficial for understanding and investigating how surface effects influence the poroelastic parameters of fluid-saturated porous materials having sufficiently small open pores.

Keywords: poroelasticity, fluid-saturated porous material, surface effects, cuboidal model, integrated bottom-up and top-down approach

1. Introduction

Fluid-saturated porous materials are plentiful in nature, engineering and biology, *e.g.*, soil, porous metal, bread, paper, and brain tissue (Hicsasmaz and Clayton, 1992; Hu et al., 2014; Su et al., 2022; Ye et al., 2016), which are typically composed of connected networks of soft solid ligaments and compressible fluid trapped in open pores. When such a porous material is loaded by external forces, the deformation of solid ligaments and the flow of fluid in the open pores influence each other. This leads to fluid-solid mechanical coupling that influences the poroelastic behavior of the porous material and, consequently, its functions (*e.g.*, load support and mass transfer). For fluid-saturated porous materials such as soil, Biot (Biot, 1941) presented his classical phenomenological theory of three-dimensional (3D) consolidation under small deformation, with surface effects neglected. Subsequently, Rice and Cleary (Rice and Cleary, 1976) reformulated Biot's constitutive relationships using macroscopic effective poroelastic parameters obtained for two limiting cases (*i.e.*, drained and undrained states), including the shear modulus, undrained and drained Poisson ratio, and Skempton pore pressure coefficient. The undrained Poisson ratio and the Skempton pore pressure coefficient describe the behavior of the porous material in undrained state when the time scale is too short and the pore fluid has no loss or gain in weight (*i.e.*, $\Delta m = 0$). In contrast, the drained Poisson ratio describes the behavior of the porous material in drained state when the time scale is long enough and the excess pore pressure is equal to its initial value (*i.e.*, $p = 0$). These macroscopic effective poroelastic parameters are dependent upon the mechanical properties of each constituent as well as the pore topological parameters of the fluid-saturated porous material, which can be obtained experimentally (Biot and Willis, 1957), or predicted theoretically by developing suitable micromechanical models (Dormieux et al., 2006).

The development of high-resolution imaging techniques *in vitro* such as atomic force microscopy (AFM), scanning electron microscopy (SEM), and transmission electron microscopy (TEM), and *in vivo* imaging systems such as magnetic resonance imaging (MRI), computed tomography (CT) and superconducting quantum interference devices (Deck et al., 1989; Jin et al., 2010), has enabled observing and characterizing pore morphologies of porous materials at micro and even nano scales. Table 1 lists representative porous materials having micro or nano scale pores. For illustration, the ligament size varies from 38 nm to 350 nm for nanoporous metal (Liu et al., 2016b; Seok et al., 2018), from 6 to 200 μm for bread (Hicsasmaz and Clayton, 1992), and from 10 to 50 μm for paper (Bennis et al., 2010). For such size scales, surface effects between solid ligaments and pore fluid are inevitable and can even play dominant roles. Surface effects are usually evaluated using a dimensionless elastocapillary number γ / ER, where γ is the surface energy, E is the Young's modulus of

the material made of solid ligaments, and R is the characteristic size of the porous material. That is, surface effects are dependent upon surface parameters, material stiffness, and morphological parameters. When $\gamma / ER \gtrsim 1$, the surface effects on the effective poroelastic parameters of a fluid-saturated porous material is no longer negligible, especially for soft materials where the stiffness of solid ligaments is close to that of the fluid filling the pores. For typical instance, γ / ER varies from 3.24×10^{-5} to 4.70×10^{-4} for nanoporous metal (Champion et al., 2019; Liu et al., 2016b; Seok et al., 2018; Shenoy, 2005), from 2.69×10^{-8} to 8.19×10^{-7} for bread (Hicsasmaz and Clayton, 1992; Sahi, 2003; Scanlon and Zghal, 2001), and from 1.65×10^{-4} to 5.05×10^{-2} for paper (Bennis et al., 2010; Eichhorn et al., 2001; Westerlind and Berg, 1988).

Built upon the mixture theory, the present authors (Chen et al., 2021) developed a theoretical model to understand and quantify the influence of surface effects on poroelastic performance of fluid-saturated porous materials. We demonstrated that, under small deformation, the classical constitutive equations of the Biot-type remain valid, at least in formality, for porous materials having sufficiently small pores (*i.e.*, surface effects are not negligible), so long as solid deformation and fluid flow at the pore level obey continuum description. Nevertheless, the effective poroelastic parameters appearing in the Biot-type constitutive equations are functions of surface effects. Therefore, to complete the constitutive modeling, additional theoretcial/numerical/experimental efforts are needed to determine the dependence of these effective poroelastic parameters upon surface effects. If relationships between effective poroelastic parameters and pore morphological parameters can be reliably established using micromechanical models, the daunting task of experimental measurements may be avoided.

In the presence of surface effects, three main types of micromechanical models have hitherto been employed to construct relationships between the microstructure and effective poroelastic parameters of a fluid-saturated porous material: the model of macromolecular network, the model of liquid inclusions, and the granular model. The macromolecular network model dated back to the pioneering studies on polymer solutions by Flory (Flory, 1942, 1953; Flory and Rehner Jr, 1943) and Huggins (Huggins, 1941), which was extended more recently by Hong et al. (Hong et al., 2008) to describe large deformation of hydrogels. Then, based on the classical inclusion theory of Eshelby (Eshelby, 1959; Eshelby, 1957) and the homogenization theory of Hill (Hill, 1965) in solid mechanics, Krichen et al. (Krichen et al., 2019) derived the effective moduli of soft composites containing liquid inclusions. For the two microstructures mentioned above, *i.e.*, polymer and liquid inclusions, the present authors quantified the effects of surface tension on the effective poroelastic parameters of fluid-

saturated porous materials in both drained and undrained states (Chen et al., 2021). Finally, built upon the classical theory of contact (Hertz, 1882; Mindlin, 1949; Walton, 1978), the effective elastic moduli of granular porous media modeled by a random distribution of identical elastic spherical solid particles were derived (Digby, 1981; Walton, 1987); the dependence of these effective elastic properties upon surface effects was subsequently evaluated, also based on the contact theory (Kendall et al., 1987; Thornton, 1993).

The macromolecular network model assumes a microstructure of free and random macromolecular chains, in which surface effects between solid and fluid act at molecular scale. The liquid inclusion model assumes a microstructure of liquid-filled pores that are closed and randomly distributed in a soft matrix, while the granular model assumes a microstructure of randomly packed elastic solid particles. For fluid-saturated cellular materials listed in Table 1, however, the three micromechanical models described above are not suitable. Therefore, establishing a new micromechanical model considering surface effects becomes a necessity, whose connected network of solid skeleton is much larger than molecular chains (*e.g.*, entanglements of molecular chains) and the pores are open (fluid-through), as opposed to closed.

In the present study, inspired by the cubic open cell model developed by Gibson and Ashby (Gibson and Ashby, 1982) for high porosity cellular foams with open cells, particular focus is placed upon establishing a micromechanical model for fluid-saturated porous materials having cellular morphologies, such as those shown in Table 1. The cubic open cell model was originally proposed to estimate the macroscopic mechanical behaviors of an idealized cellular foam by considering the bending and tension of its solid ligaments to describe the stress state of a real foam, the latter exhibiting a cellular morphology similar to those of the porous materials shown in Fig. 1. Subsequently, the cubic open cell model was applied to investigate hierarchical porous solids (Lakes, 1993), cancellous bones (Gibson, 1985), and even nanoporous metallic foams (Feng et al., 2009; Xia et al., 2011a), with surface effects characterized using the surface stress model of Gurtin and Murdoch (Gurtin and Murdoch, 1975)). In addition to mechanical analysis, the cubic open cell model (and its variations) has also been adopted by the present authors to study convective heat transfer, effective thermal conductivity, and sound absorption of open-cell metallic foams (Dupère et al., 2005; Lu et al., 1998; Lu et al., 2013). However, existing studies based on the cubic open cell model all ignored solid-fluid mechanical coupling when surface effects are no longer negligible; in addition, while existing studies focused on isotropic porous materials, biological porous materials usually exhibit highly anisotropic microstructures (Ambrosi et al., 2011; Bischoff et al., 2002; O'Shea et al., 2019). In the present study, to squarely address these issues, we first develop a micromechanics model of cuboidal open cell considering fluid pressure to estimate, from bottom-up, the effective poroelastic parameters of orthotropic fluid-saturated porous materials with surface effects. Subsequently, together with our

phenomenological constitutive model developed on the basis of homogenization and balance laws (Chen et al., 2021), we integrate the bottom-up and top-down approaches to quantify, for illustration, how surface effects influence the stress versus strain response of a fluid-saturated porous material subjected uniaxial and multiaxial external loadings as well as the stress concentration of a compressible liquid inclusion with surface tension (*e.g.*, a cell) embedded in a fluid-saturated porous material with surface effects.

The paper is organized as follows. Built upon the theoretical framework developed in our previous study (Chen et al., 2021) for fluid-saturated porous materials under surface effects, Section 2 presents, from top-down, the linear constitutive equations of anisotropic fluid-saturated porous materials with surface effects and, for isotropic porous materials, the commonly adopted relationships among a wide variety of poroelastic parameters. Section 3 presents first the cuboidal open cell model for orthotropic porous materials saturated with compressible fluid, and then applies the model to estimate, from bottom-up, the effective poroelastic parameters of the porous material in drained and undrained states. In Section 4, the influence of surface parameters and fluid compressibility on these effective poroelastic parameters is quantified. For illustration, the constitutive relationships obtained by integrating the top-down and bottom-up approaches are adopted to calculate the stress versus strain behavior of fluid-saturated porous material subjected to uniaxial tension and non-proportional multiaxial tension, in both undrained and drained states. The proposed model is further utilized to calculate the stress concentration of a small compressive liquid inclusion embedded in a fluid-saturated porous material. Although this problem is important for a range of geological, biological and engineering applications, a theoretical solution is yet hitherto unavailable due to challenges in mathematical modeling, as not only surface tension of liquid inclusion but also surface effects (surface moduli and residual surface stress) in porous material need to be accounted for. Finally, in Section 5, a discussion of the cuboidal open cell model is presented and challenging issues for extending the model to complex biological systems are raised.

2. Theoretical framework of constitutive modeling for fluid-saturated porous materials with surface effects

Built upon the classical mixture theory and the homogenization approach, the present authors developed a theoretical framework to characterize surface effects on poroelastic behaviors of fluid-saturated porous materials (Chen et al., 2021). In addition to solid and fluid phases, the fluid-solid interface was modeled as a third phase of zero thickness and zero mass. Figure 2 outlines the framework in terms of balance of mass, balance of momentum for each phase, balance of energy, and the second law of thermodynamics. With the solid phase attached with fluid-solid surface taken as a particular type of solid, we proved that the

constitutive equations of poroelastic materials exhibit the same form as those without considering surface effects (Coussy et al., 1998). In particular, for small deformation of anisotropic fluid-saturated porous materials, the linearized form of constitutive equations can be expressed as (Chen et al., 2021):

$$\begin{aligned} \sigma_{ij} &= M^{u}_{ijkl}\varepsilon_{kl} - M\alpha_{ij}\zeta, \\ p &= M\left(\zeta - \alpha_{ij}\varepsilon_{ij}\right), \end{aligned} \tag{1}$$

where σ_{ij} is the stress, ε_{ij} is the strain, p is the fluid pressure, ζ is the fluid variation, M^{u}_{ijkl} is the modulus tensor under undrained state (*i.e.*, when the fluid cannot flow out of the porous media, yielding $\Delta m = 0$), which has 21 coefficients (same as the modulus tensor for an anisotropic elastic solid), M is the Biot modulus, and α_{ij} is the Biot coefficient of effective stress. The Biot coefficient relates the volume change of fluid to the volume change of a porous material element under drained state, *i.e.*, when excess fluid pressure is completely released such that $p = 0$, and has 6 coefficients (Cheng, 1997). We must point out that, while the constitutive equations presented above are identical in formality to the classical Biot's constitutive equations, the poroelastic parameters appearing in Eq. (1) are all functions of surface effects.

In addition to the poroelastic parameters for undrained state presented in Eq. (1), there exist alternative poroelastic coefficients such as the drained moduli. In the following, the constitutive equations of (1) are re-expressed using the drained moduli. With fluid variation ζ replaced by pore pressure p, the constitutive equation for stress can be rewritten in terms of strain, as:

$$\sigma_{ij} = \left(M^{u}_{ijkl} - M\alpha_{ij}\alpha_{kl}\right)\varepsilon_{kl} - \alpha_{ij}p, \tag{2}$$

The term $M^{u}_{ijkl} - M\alpha_{ij}\alpha_{kl}$ can be expressed as M^{d}_{ijkl}, which stands for the drained modulus tensor:

$$M^{d}_{ijkl} = M^{u}_{ijkl} - M\alpha_{ij}\alpha_{kl}. \tag{3}$$

It follows that Eq. (2) can be rewritten as:

$$\sigma_{ij} = M^{d}_{ijkl}\varepsilon_{kl} - \alpha_{ij}p. \tag{4}$$

For isotropic porous materials, the constitutive equations simplify to (Chen et al., 2021):

$$\begin{aligned} \sigma_{ij} &= \left(K_u - \frac{2}{3}G\right)\varepsilon_{kk}\delta_{ij} + 2G\varepsilon_{ij} - M\alpha\zeta\delta_{ij}, \\ p &= M\left(\zeta - \alpha\varepsilon_{ii}\right), \end{aligned} \tag{5}$$

where K_u is the undrained bulk modulus, G is the shear modulus (same in drained and undrained states), M is the Biot modulus, and α is the Biot coefficient of effective stress. In addition, Eq. (4) becomes:

$$\sigma_{ij} = \left(K_d - \frac{2}{3} G \right) \varepsilon_{kk} \delta_{ij} + 2G\varepsilon_{ij} - \alpha p \delta_{ij}, \tag{6}$$

where K_d is the drained bulk modulus.

For anisotropic porous materials, three types of poroelastic parameter - M_{ijkl}^u, M and α_{ij} under undrained state or M_{ijkl}^d, M and α_{ij} under drained state - completely govern the mechanical behavior under small deformation, for other poroelastic parameters can be obtained using these parameters. To introduce poroelastic parameters other than those presented above, the strains are expressed as functions of stresses as:

$$\varepsilon_{ij} = C_{ijkl}^u \sigma_{kl} + \frac{1}{3} B_{ij} \zeta, \tag{7}$$

$$\zeta = C \left(p + \frac{1}{3} B_{ij} \sigma_{ij} \right), \tag{8}$$

where C_{ijkl}^u is the undrained compliance tensor, C is a kind of storage coefficient (defined as fluid variation per unit fluid pressure in a unit volume of porous material under zero stresses), and B_{ij} is the Skempton pore pressure coefficient that describes the relationship between the change of fluid pressure and the change of applied stress (Rice and Cleary, 1976; Skempton, 1954). In terms of the drained compliance tensor C_{ijkl}^d, Eq. (7) can be rewritten as:

$$\varepsilon_{ij} = C_{ijkl}^d \sigma_{kl} + \frac{1}{3} C B_{ij} p. \tag{9}$$

For isotropic porous materials, Eqs. (7) and (8) simplify to:

$$\varepsilon_{ij} = -\frac{1}{2G} \frac{3K_u - 2G}{9K_u} \sigma_{kk} \delta_{ij} + \frac{1}{2G} \sigma_{ij} + \frac{B}{3} \zeta \delta_{ij}, \tag{10}$$

$$\zeta = C \left(p + \frac{1}{3} B \sigma_{ii} \right). \tag{11}$$

while Eq. (9) becomes:

$$\varepsilon_{ij} = -\frac{1}{2G} \frac{3K_d - 2G}{9K_d} \sigma_{kk} \delta_{ij} + \frac{1}{2G} \sigma_{ij} + \frac{1}{3} CBp \delta_{ij}. \tag{12}$$

For isotropic porous materials, four poroelastic parameters - K_u, G, M, α or K_d, G, M, α - completely govern the mechanical behaviors. In addition to the drained bulk modulus K_d, the undrained bulk modulus K_u, the Biot coefficient of effective stress α, the Biot modulus M, and the Skempton pore pressure coefficient B, alternative poroelastic parameters having different physical meanings have also been introduced, such as the drained Poisson ratio ν, the undrained Poisson ratio ν_u, the poroelastic stress coefficient η, which relates the increment of fluid pressure to the poroelastic confining stress developed (Cheng et al., 1993), and another storage coefficient S, defined as fluid variation in a unit volume of a porous material per unit fluid pressure under uniaxial strain and constant normal stress in the strain direction (Green and Wang, 1990; Mathias et al., 2019).

Table 2 summarizes relationships among a wide variety of poroelastic parameters that have been proposed for isotropic porous materials saturated with fluid: the first column contains parameters found in poroelasticity, while the first row contains several combinations of poroelastic parameters often used in poroelasticity.

In the section to follow, with surface effects accounted for, we propose a cuboidal open cell model to describe specific microstructures of fluid-saturated porous materials listed in Table 1. The cuboidal model is then adopted to estimate from bottom-up the effective poroelastic parameters appearing in Eqs. (1) and (4), or Eqs. (5) and (6), derived from top-down for isotropic porous materials, thus completing the constitutive modeling.

3. Cuboidal open cell model and effective poroelastic parameters with surface effects

In this section, for anisotropic porous materials saturated with compressible fluid, we adopt a bottom-up approach to determine explicitly the effective poroelastic parameters appearing in phenomenological constitutive equations presented above. Firstly, in Section 3.1, inspired by the cubic open cell model (Gibson and Ashby, 1982), cellular microstructures of fluid-saturated porous materials listed in Table 1 are described and idealized using a cuboidal open cell model. Secondly, in Section 3.2, as deformations of the idealized porous material are largely dictated by solid ligaments constituting the cuboidal cell, stretching/bending of a single ligament with both residual surface stress and surface moduli accounted for is analyzed. Finally, in Section 3.3, based upon the results of ligament deformation, effective poroelastic parameters are explicitly determined as functions of porosity, surface parameters, and fluid compressibility.

3.1 Cuboidal open cell model

The fluid-saturated porous materials of Table 1 exhibit complex cellular structures such that, under external loading, solid ligaments constituting the open-cell network experience both bending and stretching deformations. For high porosity cellular solids with open cells, such as metallic foams, Gibson and Ashby (Gibson and Ashby, 1982) proposed a cubic open cell model to consider bending/stretching displacements of solid ligaments and then used the theoretical results to calculate the dependence of effective mechanical properties, such as stiffness and strength, on key morphological parameters. In the present study, built upon this conception, to simplify the analysis of anisotropic fluid-saturated porous materials, we propose a cuboidal open cell model in which a ligament connecting to the middle of another ligament is assumed to account for both bending and stretching deformations, as shown in Fig. 3(a).

Three aspects should be noted about the proposed cuboidal open cell model. Firstly, the model is similar to the Gibson-Ashby model, but different from the cubic open cell model developed by the present authors (Lu et al., 1998) for heat transfer in metallic foams. The latter does not need to consider ligament bending and hence connecting one ligament to the middle of another is not necessary as in the Gibson-Ashby model. Secondly, due to the anisotropic (orientation-dependent) material properties of several porous materials, for instance, porous hydroxyapatite (HA) scaffolds (Silva et al., 2006), the fluid-saturated porous material with open pores is idealized as a 3D lattice structure consisting of a cuboidal array (having different lengths along three orthogonal directions) of solid ligaments, with the pores filled with compressible fluid; further, for simplicity, identical uniform ligaments having axial length L and a square cross-section with side length t is assumed (alternative cross-sectional shapes can of course be considered, but not analyzed in the current study). While the cuboidal model can be used to describe orthotropic porous materials, it can be degenerated into transverse isotropic and isotropic cases by simply altering ligament lengths. Thirdly, to further simplify the problem, small elastic deformation is assumed, the deformation of nodes and the fracture of ligaments are neglected, and each ligament experiencing bending is assumed to satisfy clamped-clamped boundary condition.

It should be pointed out that, from the view of poromechanics, the properties of the pore-filling fluid significantly influence the mechanical performance of the porous material. However, as illustrated in the following sections, particular focus of this study is placed upon two limiting quasi-static states, *i.e.*, the drained state and the undrained state. Consequently, the fluid filling the pores of a porous material affects its mechanical behavior only via fluid-solid surface parameters and fluid compressibility, which are the key issues described in Sections 3.2 and 3.3.2, respectively.

3.2 Deformation of solid ligaments

To calculate the effective poroelastic parameters of the cuboidal structure depicted in Fig. 3(a), the influence of surface effects on ligament stretching/bending are firstly determined. Under external loading, two different kinds of solid ligaments are present in the cuboidal cell, *i.e.*, ligaments under axial tensile force F and ligaments under transverse concentrated force F.

For soft materials having nano and micro structures (Style et al., 2017; Wang et al., 2011), it has been established that deformation of the material is dependent significantly upon surface effects. To describe mathematically such surface effects, Gurtin and Murdoch (Gurtin and Murdoch, 1975, 1978) established a surface stress model by assuming that the surface is a negligibly thin object that adheres to the bulk without slipping. Surface moduli are then introduced to describe the stiffness properties of the surface, which are distinct from those of the bulk material, since atoms at and near a solid's surface face a different local environment than those further away (Nix and Gao, 1998; Wang et al., 2011). Besides, due to the existence of residual surface stress (*i.e.*, surface tension), a stress component perpendicular to the surface is present once it is deformed. It follows that the surface stresses can be written as (Gurtin and Murdoch, 1975, 1978):

$$\begin{aligned}\sigma_{\alpha\beta}^{s} &= \tau_s\delta_{\alpha\beta} + \left(\tau_s + \lambda_s\right)\varepsilon_{\gamma\gamma}\delta_{\alpha\beta} + 2\left(\mu_s - \tau_s\right)\varepsilon_{\alpha\beta} + \tau_s u_{\alpha,\beta}^{s},\\ \sigma_{\alpha 3}^{n} &= \tau_s u_{3,\alpha}^{s},\end{aligned} \tag{13}$$

where α and β are the in-plane coordinates, 3 is the normal direction of the plane, λ_s and μ_s are the surface moduli, which represent stress required for per unit strain, and τ_s is the residual surface stress, which can be viewed as the surface energy.

With the effects of surface stresses accounted for, the axial strain of a ligament loaded by tensile force F can be obtained, as (Feng et al., 2009):

$$\varepsilon = \frac{F}{E_m^{eff} A}, \tag{14}$$

where $A = t^2$ is the cross-sectional area and $E_m^{eff} = E_m + 4\dfrac{\lambda_s + 2\mu_s}{t}$ is the effective Young's modulus of the ligament, where the first term E_m is the Young's modulus of the material make of the ligament and the second term is caused by surface moduli.

Next, to determine the deformation of a ligament under bending, *e.g.*, under a concentrated force F at its middle point, how to describe theoretically the ligament (beam) should be firstly determined on the basis of its aspect ratio L/t. According to the proposed cuboidal model, for isotropic porous materials, the porosity ϕ is given by:

$$\phi = 1 - \frac{18Lt^2 + 8t^3}{(2L + 2t)^3}, \tag{15}$$

where the second term on the right-hand side is the volume fraction of solid. For a porous material with high porosity (*e.g.*, $\phi > 98\%$), its ligaments satisfy $L/t > 10$ and hence could be considered as slender beams, *i.e.*, the Euler-Bernoulli beam. In reality, however, the porosities of common fluid-saturated porous materials are considerably lower, varying usually between 60% and 90% (Fig. 1). For example, the porosity is about 35-75% for nanoporous metal (Liu et al., 2016b; Seok et al., 2018), 88-93% for bread (Scanlon and Zghal, 2001), and 57.1-73.6 % for paper (Tanpichai et al., 2019). For such porous materials, the ligaments need to be considered as stubby beams (*i.e.*, the Timoshenko beam with an aspect ratio of $L/t \le 10$) such that the effect of shear deformation is accounted for (Hutchinson, 2001).

Based on the Gurtin-Murdoch model of surface stress, the mechanical behavior of a nanobeam under surface effects has been studied in recent years. For instance, with surface stress taken as a distributed force, explicit solutions of a Euler-Bernoulli beam were obtained (He and Lilley, 2008) for different boundary conditions: fixed-fixed, cantilever, and simply supported; similarly, analytical solutions for both transverse vibration and axial buckling of a Timoshenko beam under surface effects were obtained (Wang and Feng, 2009). Nonetheless, in these studies, the Poisson effect induced by surface stress (Lu et al., 2006) was neglected, which may significantly influence the mechanical behavior of the beam. With such Poisson effect induced by surface stressing accounted for, closed-form theoretical solutions for the static response and free vibration of both Euler and Timeshenko beams were obtained by analyzing the force equilibrium of an incremental beam (bulk) element (Liu and Rajapakse, 2009). Further, postbuckling of a Timoshenko beam was analyzed using the principle of virtual work (Ansari et al., 2014). In the present study, based on a previous work (Liu and Rajapakse, 2009), we analyze a Timoshenko beam by considering both surface stress and Poisson effect to calculate the deformation experienced by each bending ligament in the cuboidal model of Fig. 3(a).

For a Timoshenko beam with surface effects as depicted in Fig. 3(b), let *x* represent the axial direction, and let *y* and *z* denote the directions orthogonal to the axial direction. For simplification, the surface stresses are modeled as distributed forces on the beam, which are deformation dependent in subsequent analysis of incremental beam element. Consequently, the surface stresses may be expressed as (Liu and Rajapakse, 2009):

$$\sigma_{xx}^{s} = (\lambda_s + 2\mu_s)u_{x,x} + \tau_s, \quad \sigma_{xz}^{n} = \tau_s u_{x,z}, \tag{16}$$

where σ_{xx}^{s} and σ_{xz}^{n} represent the stress along the *x* direction and the direction perpendicular to the surface, respectively, and u_x is the displacement along the *x* direction.

Equations governing the bending deformation of a Timoshenko beam with surface effects can be written as (Ansari et al., 2014):

$$Q+\frac{d\left(M_{xx}+M_{xx}^{s}\right)}{dx}=0,\ \frac{d\left(Q+Q^{s}\right)}{dx}=0, \tag{17}$$

where the terms

$$M_{xx}=E_m I\frac{d\varphi}{dx}-\frac{2\nu\tau_s}{t}I\frac{d^2w}{dx^2}, \tag{18}$$

$$M_{xx}^{s}=\left(\lambda_s+2\mu_s\right)I_s\frac{d\varphi}{dx}, \tag{19}$$

are the moments considering surface stresses, in which $I=\frac{1}{12}t^4$, $I_s=\frac{2}{3}t^3$, and the terms

$$Q=kGA\left(\frac{dw}{dx}-\varphi\right), \tag{20}$$

$$Q^{s}=2t\tau_s\frac{dw}{dx}, \tag{21}$$

are separately the shear force defined in the classical beam theory and the additional shear force induced by surface stress, in which $A=t^2$.

The boundary conditions are:

$$w(0)=\varphi(0)=0,\ \varphi\left(\frac{L}{2}\right)=0,\ Q+Q^{s}=\frac{F}{2}. \tag{22}$$

Following Liu and Rajapakse (Liu and Rajapakse, 2009), for a clamped-clamped Timoshenko beam subjected to a concentrated load *F* at its center, the deflection of the beam can be obtained from Eqs. (17) and (22) as:

$$\begin{aligned} w(x)=\frac{F}{2H(H+V)\xi}\Bigg[&(H+V)\xi x+\sqrt{\frac{V}{H}}\frac{\sinh\left(\sqrt{HV}L\xi/4-\sqrt{HV}\xi x\right)}{\cosh\left(\sqrt{HV}L\xi/4\right)}\\ &-\sqrt{\frac{V}{H}}\tanh\left(\sqrt{HV}L\xi/4\right)\Bigg], \end{aligned} \tag{23}$$

where $V=kGA$, ν is the Poisson ratio, and G is the shear modulus while $H=2t\tau_s$, $\xi=\sqrt{1/\left[(EI)_{eff}(H+V)-sV\right]}$, $(EI)_{eff}=E_m I+\left(\lambda_s+2\mu_s\right)I_s$ and $s=\frac{1}{6}\nu t^3\tau_s$ are terms

modified by surface effects. The shear coefficient $k=\dfrac{5(1+\nu)}{6+5\nu}$ is introduced to estimate the shear stress acting on the cross-section of the beam, which is dependent upon beam geometry (Hutchinson, 2001). In the section to follow, the solution of (23) is used to calculate the effective poroelastic parameters.

In passing, it is worth noting that, when shear deformation of the beam is negligible (*i.e.*, shear stiffness tends to infinity, $V\to\infty$), Eq. (23) degrades to the solution for Euler-Bernoulli beams under surface effects (Liu and Rajapakse, 2009):

$$w(x)=\frac{F}{2H\xi_1}\left[\xi_1 x+\frac{1}{\sqrt{H}}\frac{\sinh\left(\sqrt{H}L\xi_1/4-\sqrt{H}\xi_1 x\right)}{\cosh\left(\sqrt{H}L\xi_1/4\right)}-\frac{1}{\sqrt{H}}\tanh\left(\sqrt{H}L\xi_1/4\right)\right]. \quad (24)$$

where $\xi_1=\sqrt{1/\left[(EI)_{eff}-s\right]}$. Further, in the absence of surface effects (*i.e.*, $\tau_s=\lambda_s=\mu_s=0$), Eq. (23) becomes the classical solution for Timoshenko beams:

$$\begin{aligned} w(x)&=Fx\left[\frac{(3L-4x)x}{48EI}+\frac{1}{2V}\right],\\ \varphi(x)&=Fx\frac{L-2x}{8EI}. \end{aligned} \quad (25)$$

while Eq. (24) becomes the classical solution for Euler-Bernoulli beams:

$$w(x)=Fx^2\frac{3L-4x}{48EI}. \quad (26)$$

3.3 Effective poroelastic parameters

The proposed cuboidal model detailed in Section 3.1 represents an orthotropic fluid-saturated elastic porous material having open (fluid-through) cells. Correspondingly, the macroscopic effective modulus tensor M^u_{ijkl} (or M^d_{ijkl}) has nine independent coefficients, the Biot coefficient of effective stress α_{ij} (which describes relationship between the volume change of fluid in pore and that of the element under drained state) has one independent coefficient, and the Biot modulus M (which describes the relationship between fluid pressure and fluid variation under constant volumetric strain) has one independent coefficient (Cheng, 1997). For a transversely isotropic or isotropic fluid-saturated porous material, its effective poroelastic parameters can be obtained by altering ligament length(s) in the cuboidal model. For a transversely isotropic porous material, the modulus tensor M^u_{ijkl} (or M^d_{ijkl}) has five independent coefficients, while the Biot coefficient α_{ij} has two coefficients. For an

isotropic porous material, the modulus tensor M_{ijkl}^{u} (or M_{ijkl}^{d}) has two coefficients and the Biot coefficient α_{ij} has only one coefficient.

Next, the deformations of solid ligaments in the cuboidal model are obtained to calculate the effective poroelastic parameters detailed above. For a fluid-saturated porous material, its mechanical response possesses two limiting states, namely, the drained state when excess pore pressure vanishes and the undrained state when the fluid cannot escape the pore of the material. Inspired by the classical work of Rice and Cleary (Rice and Cleary, 1976), the present study lays a strong emphasis on obtaining effective poroelastic parameters in two limiting states, as other types of effective parameter can be obtained using the drained and undrained parameters. In the following, the drained Young's moduli are derived first, which are then used to derive the undrained Young's moduli. In addition to the drained and undrained moduli, key poroelastic parameters representing fluid-solid coupling are also obtained.

3.3.1 Drained Young's moduli

For the drained state, Xia et al. (Xia et al., 2011a; Xia et al., 2011b) calculated the effective Young's modulus using the isotropic unit cell model shown in Fig. 3(a); they considered bending and axial displacements of solid ligaments (beams) under surface stress, but neglected Poisson effect due to surface stress. To obtain the effective drained moduli for more general cases (*e.g.*, material anisotropy and Poisson effect induced by surface stress), the stresses and strains of the proposed cuboidal model need to be calculated.

When the cuboidal model is subjected to uniaxial tension (compression), its stresses and strains can be obtained straightforwardly. Specifically, with a volume of $V_{cell}=2\left(L_x+t\right)\cdot 2\left(L_y+t\right)\cdot 2\left(L_z+t\right)$, the cuboidal cell of Fig. 3(a) is subjected to a tensile force $F_z=2\sigma_z\left(L_x+t\right)\left(L_y+t\right)$ acting along the *z* direction, leading to an axial stress given by:

$$\sigma_z=\frac{F_z}{2\left(L_x+t\right)\left(L_y+t\right)}. \tag{27}$$

It follows that the effective Young's modulus of the cell is:

$$E_{d,z}=\frac{\sigma_z}{\varepsilon_z}=\frac{F_z}{2\left(L_x+t\right)\left(L_y+t\right)\varepsilon_z}, \tag{28}$$

where the strain ε_z is calculated as:

$$\varepsilon_z=\frac{\varepsilon_{L_z/2}L_z+\varepsilon_{L_z}\left(L_z+2t\right)+w\left(L_x/2\right)}{2\left(L_z+t\right)}, \tag{29}$$

This strain is consisted of three parts: (i) tensile strain $\varepsilon_{L_z} = \frac{F_z}{2E_m^{eff}A}$ of beam with length $L_z + 2t$, (ii) tensile strain $\varepsilon_{L_z/2} = \frac{F_z}{E_m^{eff}A}$ of beam with length $L_z/2$, and (iii) deflection $w(L_x/2)$ at the middle of bending beam with length L_x, which can be obtained via Eq. (23). The effective drained Young's modulus can then be obtained as:

$$E_{d,z} = \frac{1}{(L_x+t)(L_y+t)} \frac{2E_m^{eff}H^{\frac{3}{2}}(H+V)(L_z+t)}{\sqrt{H}\left(3HL_z+2Ht+E_m^{eff}L_x\right)(H+V) - \frac{4E_m^{eff}\sqrt{V}}{\xi}\tanh\left(\frac{\xi\sqrt{HV}L_x}{4}\right)}. \quad (30)$$

Following similar procedures, the drained Young's moduli for the *y* and *x* directions, $E_{d,y}$ and $E_{d,x}$, are determined. When the ligaments along three orthogonal directions (*i.e.*, *x*, *y* and *z*) have identical lengths, the model becomes isotropic, yielding $E_{d,z} = E_{d,y} = E_{d,x}$.

Due to the topological properties of the cuboidal model (Hedayati et al., 2018), the bending beams experience no axial deformation and hence the effective Poisson ratios

$$\nu_{d,zy} = \nu_{d,zx} = \nu_{d,yx} = 0. \quad (31)$$

To obtain the effective shear modulus G_{zx}, a tensile stress σ_z and a compressive stress σ_x are applied simultaneously along the *z* and *x* directions, thus enabling the strains of the two directions to satisfy $\varepsilon_z = -\varepsilon_x$. It follows that G_{zx} can be calculated by (Li et al., 2006):

$$G_{zx} = \frac{\sigma_z - \sigma_x}{2(\varepsilon_z - \varepsilon_x)}, \quad (32)$$

where the stresses (σ_z, σ_x) and the strains (ε_z, ε_x) can be obtained using the method analogous to that detailed above. The other two shear moduli, G_{yz} and G_{xy}, are similarly obtained, as:

$$G_{yz} = \frac{\sigma_y - \sigma_z}{2\left(\varepsilon_y - \varepsilon_z\right)},$$
$$G_{xy} = \frac{\sigma_x - \sigma_y}{2\left(\varepsilon_x - \varepsilon_y\right)}. \tag{33}$$

Finally, the drained modulus tensor of Eq. (4) is expressed using the nine parameters obtained hitherto for orthotropic porous materials, *i.e.*, $E_{d,z}, E_{d,y}, E_{d,x}, \nu_{d,zy}, \nu_{d,zx}, \nu_{d,yx}, G_{zx}$, G_{yz}, and G_{xy}, as:

$$M^d_{1111} = \frac{E_{d,x}E_{d,y}\left(E_{d,z} - E_{d,y}\nu^2_{d,zy}\right)}{A},$$
$$M^d_{2222} = \frac{E^2_{d,y}\left(E_{d,z} - E_{d,x}\nu^2_{d,zx}\right)}{A},$$
$$M^d_{3333} = \frac{E^2_{d,z}\left(E_{d,y} - E_{d,x}\nu^2_{d,yx}\right)}{A},$$
$$M^d_{1122} = M^d_{2211} = \frac{E_{d,x}E_{d,y}\left(E_{d,z}\nu_{d,yx} + E_{d,y}\nu_{d,zx}\nu_{d,zy}\right)}{A},$$
$$M^d_{1133} = M^d_{3311} = \frac{E_{d,x}E_{d,y}E_{d,z}\left(\nu_{d,zx} + \nu_{d,yx}\nu_{d,zy}\right)}{A}, \tag{34}$$
$$M^d_{2233} = M^d_{3322} = \frac{E_{d,y}E_{d,z}\left(E_{d,x}\nu_{d,yx}\nu_{d,zx} + E_{d,y}\nu_{d,zy}\right)}{A},$$
$$M^d_{1212} = G_{xy},$$
$$M^d_{2323} = G_{yz},$$
$$M^d_{1313} = G_{zx},$$

where $A = E_{d,y}E_{d,z} - E_{d,x}E_{d,z}\nu^2_{yx} - E_{d,x}E_{d,y}\nu^2_{zx} - E^2_{d,y}\nu^2_{d,zy} - 2E_{d,x}E_{d,y}\nu_{d,yx}\nu_{d,zx}\nu_{d,zy}$.

3.3.2 Undrained Young's moduli and Poisson ratio

In this section, the method based on the cuboidal model (*i.e.*, unit cell) considering fluid pressure is adopted to calculate the undrained poroelastic parameters for fluid-saturated porous materials that exhibit cellular microstructures similar to open-celled foams. Note that, for the undrained state, the time scale is too short to allow the fluid to escape from an element to neighboring elements of the porous material, *i.e.*, there is no loss or gain of fluid in the unit cell model. Nonetheless, the time scale is long enough to allow the fluid pressure and solid stress to be balanced within the elements constituting a 'point' in the continuum model of the porous material (Rice and Cleary, 1976). Therefore, besides the external force *F*, the deformation of the unit cell is also influenced by fluid pressure, which depends on solid-fluid

coupling in the unit cell when F is applied. In the following, the volume change induced by both the external force and fluid pressure is determined first, and relationships between the strains of the unit cell and the fluid pressure are derived. The effective moduli and Poisson ratio of the unit cell are then expressed by the strains of the unit cell. Finally, the effective moduli and Poisson ratio are calculated by solving the resulting simultaneous equations.

For an orthotropic fluid-saturated porous material, the undrained Young's modulus along the z direction is determined by:

$$E_{u,z} = \frac{\varepsilon_{F_z} E_{d,z} - p}{\varepsilon_z} \tag{35}$$

where $\varepsilon_{F_z} E_{d,z}$ is the stress under drained state, and ε_z is the total strain of the unit cell experiencing tensile force and fluid pressure. In the present study, in order to obtain results with general applicability, the fluid is assumed to be linearly compressible (Chen et al., 2018; Detournay and Cheng, 1993) while the pressure p is expressed as

$$p = -K_f \frac{\Delta V_f}{V_f}, \tag{36}$$

where K_f is the fluid bulk modulus, and ΔV_f and V_f are separately the volume change and initial volume of fluid, respectively.

Due to the additional deformation of solid beams by fluid pressure, the effective bulk modulus of the beam should be defined. Under hydrostatic loading, as the linear strain in one direction is ε and the volumetric strain is 3ε, force balance dictates that:

$$3K_m^{eff}\varepsilon t^2 = 3K_m\varepsilon t^2 + 4\left(\lambda_s + \mu_s\right)\varepsilon t, \tag{37}$$

where K_m is the solid bulk modulus. The effective bulk modulus of the beam can be written as:

$$K_m^{eff} = K_m + \frac{4}{3}\frac{\lambda_s + 2\mu_s}{t}. \tag{38}$$

In addition, the effective Poisson ratio of the beam can be defined as:

$$\nu_m^{eff} = \frac{1}{2}\left(1 - \frac{E_m^{eff}}{3K_m^{eff}}\right). \tag{39}$$

When the unit cell is subjected to a tensile force $F_z = 2\sigma_z\left(L_x + t\right)\left(L_y + t\right)$ along the z direction, the total strain ε_z is:

$$\varepsilon_z = \varepsilon_{F_z} + \varepsilon_p, \tag{40}$$

where ε_{F_z} is the strain caused by the tensile force and ε_p is the linear strain of the beam induced by fluid pressure:

$$\varepsilon_p = -\frac{p}{3K_m^{eff}}. \tag{41}$$

From Eq. (28), the balance of tensile forces leads to:

$$2F_z = \varepsilon_{F_z} E_{d,z} \left(2L_x + 2t\right)\left(2L_y + 2t\right). \tag{42}$$

The fluid pressure p can be rewritten as:

$$\begin{aligned} p &= -K_f \frac{\Delta V_f}{V_f} = -K_f \frac{\Delta V_{cell} - \Delta V_m}{V_f} \\ &= -K_f \frac{V_{cell}\varepsilon_z \left(1 - \nu_{u,zy} - \nu_{u,zx}\right) - \Delta V_m}{V_f}, \end{aligned} \tag{43}$$

where ΔV_{cell} is the total volume change of unit cell, ΔV_m is the volume change of solid matrix, and $\nu_{u,zy}$ and $\nu_{u,zx}$ are two effective undrained Poisson ratios along *zy* and *zx* directions for orthotropic fluid-saturated porous materials.

It should be noticed that, upon applying the tensile force F_z, the pressure p is applied to the *y* and *x* directions of the unit cell due to the influence of fluid, and hence the unit cell is not under the state of uniaxial tension. To ensure uniaxial tension, opposing pressure $-p$ acting on the unit cell along *x* and *y* directions needs to be applied. Therefore, the volume change of solid matrix is consisted of three parts: volume change caused by tensile forces $\Delta V_{m,F_z}$, volume change caused by pressure $\Delta V_{m,p}$, and volume change caused by opposing pressure $\Delta V_{m,-p}$. The volume change caused by tensile forces $\Delta V_{m,F_z}$ can be calculated as:

$$\begin{aligned}\Delta V_{m,F_z} &= \left[2\varepsilon_{L_z/2}L_z + 4\varepsilon_{L_z}\left(L_z+2t\right)\right]t^2\left(1-2\nu_m^{eff}\right)\\ &= 4\left(L_z+t\right)\left(1-2\nu_m^{eff}\right)t^2\frac{F_z}{E_m^{eff}t^2}\\ &= 4\left(L_z+t\right)\left(1-2\nu_m^{eff}\right)\frac{1}{E_m^{eff}}\frac{1}{2}E_{d,z}\varepsilon_{F_z}\left(2L_x+2t\right)\left(2L_y+2t\right)\\ &= \frac{E_{d,z}\varepsilon_{F_z}}{E_m^{eff}}V_{cell}\left(1-2\nu_m^{eff}\right)\\ &= \frac{E_{d,z}}{E_m^{eff}}V_{cell}\left(1-2\nu_m^{eff}\right)\left(\varepsilon_z+\frac{p}{3K_m^{eff}}\right)\\ &= \frac{V_{cell}}{3K_m^{eff}}E_{d,z}\left(\varepsilon_z+\frac{p}{3K_m^{eff}}\right),\end{aligned} \tag{44}$$

where $E_{d,z}\left(\varepsilon_z+\frac{p}{3K_m^{eff}}\right)$ can be considered as the stress caused by tensile force F_z.

The volumetric change of the solid caused by pressure $\Delta V_{m,p}$ is given by:

$$\Delta V_{m,p} = -\frac{p}{K_m^{eff}}V_s = -\frac{p}{K_m^{eff}}V_{cell}\left(1-\phi\right). \tag{45}$$

The volumetric change $\Delta V_{m,-p}$ caused by opposite pressure can be obtained by setting $E_{d,z}\left(\varepsilon_z+\frac{p}{3K_m^{eff}}\right)=p$ in Eq. (44), as:

$$\Delta V_{m,-p} = 2\frac{V_{cell}}{3K_m^{eff}}p. \tag{46}$$

According to Eqs. (44)-(46), the total volume change of the solid beam can be obtained as:

$$\begin{aligned}\Delta V_m &= \Delta V_{m,F_z} + \Delta V_{m,p} + \Delta V_{m,-p}\\ &= \frac{E_{d,z}}{3K_m^{eff}}V_{cell}\varepsilon_z + p\frac{V_{cell}}{K_m^{eff}}\left[\frac{1}{3}\left(\frac{E_{d,z}}{3K_m^{eff}}+2\right)-\left(1-\phi\right)\right].\end{aligned} \tag{47}$$

Substituting (47) into (43) yields:

$$\frac{p}{\varepsilon_z} = \frac{\left(1-\nu_{u,zy}-\nu_{u,zx}\right)-\frac{E_{d,z}}{3K_m^{eff}}}{\frac{1}{3K_m^{eff}}\left(\frac{E_{d,z}}{3K_m^{eff}}+2\right)-\frac{\left(1-\phi\right)}{K_m^{eff}}-\frac{\phi}{Kf}}, \tag{48}$$

where the undrained Young's modulus can be expressed using (35), as:

$$E_{u,z}=\frac{\varepsilon_{F_z}E_{d,z}-p}{\varepsilon_z}=\frac{\left(\varepsilon_z+\dfrac{p}{3K_m^{eff}}\right)E_{d,z}-p}{\varepsilon_z}=E_{d,z}+\frac{p}{\varepsilon_z}\left(\frac{E_{d,z}}{3K_m^{eff}}-1\right). \tag{49}$$

Using similar method, we write the strains in *y* and *x* directions as:

$$\begin{aligned}\varepsilon_{F_y}&=\varepsilon_y+\frac{p}{3K_m^{eff}},\\ \varepsilon_{F_x}&=\varepsilon_x+\frac{p}{3K_m^{eff}},\end{aligned} \tag{50}$$

where ε_{F_y} and ε_{F_x} are the strains induced by the opposite pressure, given by:

$$\begin{aligned}\varepsilon_{F_y}&=\frac{p}{E_{d,y}},\\ \varepsilon_{F_x}&=\frac{p}{E_{d,x}}.\end{aligned} \tag{51}$$

The effective undrained Poisson ratios $\nu_{u,zy}$ and $\nu_{u,zx}$ can be determined by:

$$\begin{aligned}\nu_{u,zy}&=-\frac{\varepsilon_y}{\varepsilon_z},\\ \nu_{u,zx}&=-\frac{\varepsilon_x}{\varepsilon_z}.\end{aligned} \tag{52}$$

When the unit cell is subjected to a tensile force F_y in the *y* direction, the undrained Young's modulus $E_{u,y}$ and Poisson ratio $\nu_{u,yx}$ are determined by:

$$\begin{aligned}E_{u,y}&=E_{d,y}+\frac{p}{\varepsilon_y}\left(\frac{E_{d,y}}{3K_m^{eff}}-1\right),\\ \nu_{u,yx}&=-\frac{\varepsilon_x}{\varepsilon_y}.\end{aligned} \tag{53}$$

Similarly, the undrained Young's modulus $E_{u,x}$ is determined by:

$$E_{u,x}=E_{d,x}+\frac{p}{\varepsilon_x}\left(\frac{E_{d,x}}{3K_m^{eff}}-1\right). \tag{54}$$

Solving Eqs. (49) and (52)-(54) enables determining the six independent parameters for orthotropic fluid-saturated porous materials; as the fluid pressure remains unchanged under shear forces, the three undrained shear moduli are the same as the three drained ones.

Therefore, the nine undrained parameters, *i.e.*, $E_{u,z}, E_{u,y}, E_{u,x}, \nu_{u,zy}, \nu_{u,zx}, \nu_{u,yx}, G_{zx}, G_{yz}, G_{xy}$, are all determined for orthotropic cases. When $K_f = 0$, the influence of fluid pressure vanishes such that the undrained parameters degenerate into the drained parameters.

Similar with Eq. (34), the parameters appearing in the undrained modulus tensor for orthotropic cases can be expressed using the undrained moduli and undrained Poisson ratios. In the following, the influence of fluid pressure is considered to calculate the effective undrained modulus tensor.

3.3.3 Key poroelastic parameters representing fluid-solid coupling

For a fluid-saturated porous material, in addition to the standard parameters of linear elasticity, several parameters of poroelasticity are needed to characterize solid-fluid coupling. Here, two commonly applied parameters, *i.e.*, the Biot coefficient of effective stress α_i for i direction ($i = x, y, z$) and the Biot modulus M, are calculated since both parameters exhibit clear physical meanings.

The Biot coefficient α_i is defined as the ratio of fluid volumetric change in a unit cell to the total volumetric change of that cell under drained state when a load is applied in i ($i = x, y, z$) direction, namely:

$$\alpha_i = \frac{\Delta V_f}{\Delta V_{cell}} = 1 - \frac{\Delta V_m}{\Delta V_{cell}}. \tag{55}$$

Given that the drained Poisson ratios are zero (*i.e.*, $\nu_{d,zy} = \nu_{d,zx} = 0$), the volume change ΔV of the unit cell can be expressed as:

$$\Delta V_{cell} = V_{cell}\varepsilon_z \left(1 - \nu_{d,zy} - \nu_{d,zx}\right) = V_{cell}\varepsilon_z. \tag{56}$$

Substituting Eq. (44) (setting $p = 0$) into Eq. (55) yields the Biot coefficient:

$$\alpha_i = 1 - \frac{E_{d,i}}{3K_m^{eff}}. \tag{57}$$

Next, according to Eq. (1), for undrained cases (*i.e.*, $\zeta = 0$), the Biot modulus M can be defined as:

$$M = -\frac{p}{\alpha_{ij}\varepsilon_{ij}}. \tag{58}$$

For orthotropic porous materials, the Biot modulus can be expressed as

$$M = -\frac{p}{\alpha_x\varepsilon_x + \alpha_y\varepsilon_y + \alpha_x\varepsilon_x}. \tag{59}$$

Then, using Eq. (50), (51) and (57), we rewrite Eq. (59) as:

$$M=-\frac{1}{\left(1-\frac{E_{d,x}}{3K_m^{eff}}\right)\left(\frac{1}{E_{d,x}}-\frac{1}{3K_m^{eff}}\right)+\left(1-\frac{E_{d,y}}{3K_m^{eff}}\right)\left(\frac{1}{E_{d,y}}-\frac{1}{3K_m^{eff}}\right)+\left(1-\frac{E_{d,z}}{3K_m^{eff}}\right)\frac{\varepsilon_z}{p}}, \quad (60)$$

where $\frac{\varepsilon_z}{p}$ can be obtained by Eq. (48).

4. Results

Thus far, all the effective poroelastic parameters that govern the mechanical behavior of an orthotropic fluid-saturated porous material experiencing small linear elastic deformation have been obtained using a bottom-up approach, with surface effects accounted for. In this section, for the sake of analysis, only the effective poroelastic parameters for isotropic porous materials are analyzed. Firstly, the influence of surface parameters on effective drained parameters is quantified. Secondly, the influence of both surface parameters and fluid compressibility on effective undrained parameters is quantified. Finally, stress versus strain curves of the porous material in both undrained and drained states are analyzed.

4.1 Effective poroelastic parameters under drained state

Under the drained state, the effective Poisson ratio is null, and hence only the effective drained Young's modulus and the Biot coefficient of effective stress need to be determined. From Eqs. (30) and (57), the two poroelastic parameters depend on three dimensionless parameters: the porosity ϕ, the residual surface stress $\tau_s / E_m t$, and the surface moduli $\left(\lambda_s + 2\mu_s\right) / E_m t$.

The influence of residual surface stress on effective drained Young's modulus is displayed in Fig. 4(a) for different values of surface moduli. The effective drained modulus increases with the increase of surface moduli. The influence of residual surface stress can be considered as a distributed force acting on a bending beam along the opposite direction of external load (Liu and Rajapakse, 2009), as shown in Fig. 5(a). Therefore, the residual surface stress increases the effective modulus by reducing the deflection of the beam, thus increasing its effective modulus. In contrast, for a poroelastic material embedded with cylindrical compressible liquid inclusions, its effective modulus initially increases and then decreases with the increase of surface tension, *i.e.*, residual surface stress (Ti et al., 2022). The different influencing trends exhibited by residual surface stress on effective Young's modulus may be attributed to the different pore morphologies (open cell versus closed cell) considered by the present study and an earlier study (Ti et al., 2022).

For selected residual surface stresses, Fig. 4(b) reveals that the effective drained Young's modulus increases with the increase of surface moduli. Similar to residual surface stress, the influence of surface moduli can be considered as a film that enhances the effective bending stiffness EI of a beam (Liu and Rajapakse, 2009), as shown in Fig. 5(a). Besides, the surface moduli can also increase the Young's modulus of a stretched beam, as shown in Fig. 5(b). The increasing bending stiffness as well as Young's modulus induced by surface moduli can reduce the deformation of the beam under either bending or stretching, thus increasing its effective modulus.

For large residual surface stresses, it is observed that the influence of surface moduli become more significant, whereas for large surface moduli, residual surface stress plays a more significant role (Figs. 4(a, b)). This implies that certain coupling effect is present between the two surface parameters. To explain the mechanism underlying such coupling, Fig. 5 displays a beam with surface effects under loading. First, the deformation of a Timoshenko beam subjected to bending and tension is shown in Figs. 5(a, b). It can be seen from the classical result of Fig. 5(a) that, if the residual surface stress and surface moduli have similar magnitudes, the influence of residual surface stress on deformation is larger than that of surface moduli. Specifically, as the dimensionless surface parameters $a=\dfrac{\lambda_s+2\mu_s}{E_m t}$ and $b=\dfrac{\tau_s}{E_m t}$ are varied, the deflection of the bending beam varies as:

$$\begin{aligned} w\left(a=1,b=0\right)&=0.40w_{classical},\\ w\left(a=0,b=1\right)&=0.051w_{classical},\\ w\left(a=1,b=1\right)&=0.048w_{classical}, \end{aligned} \tag{61}$$

where $w_{classical}=w\left(a=0,b=0\right)$ and $\nu=0.3$. Compared with surface moduli, residual surface stress is seen to play a more dominant role in the deformation of a bending beam. For a beam under uniaxial tension (Fig. 5(b)), while surface moduli increase its Young's modulus, residual surface stress has no influence on beam deformation: that is, surface moduli dominate the deformation of a stretching beam. If the surface parameter dominating either bending or stretching has a small magnitude, its influence on the deformation and effective Young's modulus of the beam is small and, correspondingly, the other surface parameter also has little influence. In sharp contrast, the influence of one surface parameter (either surface moduli or residual surface stress) becomes significant when the other surface parameter is large. The parallel structure illustrated in Fig. 5(c) is commonly found in physics, *e.g.*, the beam displacement, surface parameter, and external load exhibit relationships similar to those among the current, electrical resistance and voltage in electricity.

Next, the proposed cuboidal model is employed to investigate the drained Young's modulus of nanoporous gold. The predicted effective drained Young's modulus is plotted in Fig. 6 as a function of the volume fraction of solid matrix ϕ_m, *i.e.*, $1-\phi$, and compared with existing experimental data (Liu et al., 2016b). The SEM image of nanoporous gold inserted in Fig. 6 shows that it exhibits a network structure consisted of approximately cylindrical solid ligaments. For the nanoporous gold samples tested (Liu et al., 2016b), the ligament size (diameter) ranges from 15 nm to 500 nm: correspondingly, the porosity varies in the range of 77%-98% (Liu et al., 2016b). Given that the microstructures of these nanoporous gold samples are intrinsically irregular, the present study provides an approximate method to estimate effective poroelastic parameters by converting the characteristic sizes of sample microstructures into dimensionless parameters. The tested samples having varying porosities also have different ligament sizes (*t*), resulting in the upper and lower bounds of dimensionless parameters $\left(\lambda_s+2\mu_s\right)/E_m t$ and $\tau_s/E_m t$. For bulk gold, the surface parameters determined via atomistic simulations are constant: $\lambda_s+2\mu_s=-5.3$ N/m and $\tau_s=1.4$ N/m (Liu et al., 2016b; Shenoy, 2005). It follows that, as the ligament size *t* is altered, $\left(\lambda_s+2\mu_s\right)/E_m t$ varies from -1.2×10^{-4} to -6.1×10^{-3} while $\tau_s/E_m t$ varies from 3.2×10^{-5} to 1.6×10^{-3}. It is seen from Fig. 6 that the present theoretical results fit well with existing experimental measurements. Further, as gold has large stiffness relative to liquid (water), the dimensionless surface parameters have small values ($<1.6\times10^{-3}$) and hence affect negligibly the effective poroelastic properties of nanoporous gold.

Figure 7(a) plots the influence of porosity on the Biot coefficient of effective stress for selected dimensionless surface parameters. The Biot coefficient is seen to increase with increasing porosity, which can be explained by the definition of the coefficient itself. With surface moduli fixed, Fig. 7(b) shows that the Biot coefficient decreases as the residual surface stress is increased. Such influence of residual surface stress on effective stress is related to the shear strength of the porous material (Khalili et al., 2004). Increasing the residual surface stress leads to larger effective modulus of the cuboidal cell and hence smaller deformation, such that pressure should be increased to ensure that the strain of the cell remains unchanged. Therefore, the change in fluid volume should be increased, thus increasing the Biot coefficient.

For selected values of residual surface stress, the results of Fig. 7(c) show that the Biot coefficient first decreases, reaching a local minimum, and then increases as surface moduli are increased. According to Eq. (57), this tendency is attributed to the fact that surface moduli

influence the effective drained Young's modulus of the unit cell (E_d) in a way different from that on the bulk modulus of solid ligament (K_m^{eff}).

4.2 Effective poroelastic parameters under undrained state

In undrained state, due to the presence of fluid pressure, the effective Poisson ratio of a fluid-saturated porous material with open cells is no longer null. Further, in undrained state, the effective Young's modulus and other parameters not only depend upon three dimensionless parameters, *i.e.*, the porosity ϕ and two surface parameters expressed as $\tau_s / E_m t$ and $\left(\lambda_s + 2\mu_s\right) / E_m t$, but also upon the bulk modulus of fluid K_f / E_m, which is similar to the results obtained for an elastic matrix embedded with compressible liquid inclusions (Chen et al., 2020; Ti et al., 2022). When surface effects are absent, the undrained parameters can be degraded into the classical results (Cheng, 1997).

The influence of porosity and fluid compressibility on the effective undrained Young's modulus for selected surface parameters are presented separately in Fig. 8(a) and (b), respectively. The undrained Young's modulus decreases with increasing porosity but increases with increasing fluid bulk modulus (due to increasing fluid pressure). The variation trends of the undrained Young's modulus with residual surface stress and surface moduli are similar to those of the drained Young's modulus shown in Fig. 7.

The effective undrained Poisson ratio increases with the increase of the porosity (Fig. 9(a)). To ensure the strain experienced by the unit cell remains unchanged, the external load should be reduced due to the decrescent undrained Young's modulus induced by increasing porosity, the latter causing decreased volume change of solid ligaments. The larger fluid pressure induced by increased volume change of fluid leads to larger lateral deformation of the unit cell. When the porosity of the porous material tends to 1.0, the undrained Poisson ratio approaches to the limit of 0.5, which means the fluid volume has no change in the limiting case.

The influence of fluid bulk moduli on the effective undrained Poisson ratio is depicted in Fig. 9(b) for chosen surface parameters. The undrained Poisson ratio increases with the increase of fluid bulk modulus, for the latter leads to larger fluid pressure. As shown further in Figs. 9(c, d), the undrained Poisson ratio decreases with the increase of the residual stress or surface moduli. Again, for the case of fixed strain of unit cell, since increasing either the residual surface stress or surface moduli increases the effective undrained Young's modulus, the external load should be increased and, correspondingly, the volume change of the solid also increases. As a result, lateral deformation of the unit cell is reduced, for the smaller fluid volume change enables the fluid pressure to decrease.

Finally, the results of Fig. 10(a) reveal that the effective Biot modulus decreases with increasing porosity for relatively small fluid bulk modulus, *e.g.*, $K_f / K_m = 0.01$, but increases with porosity for larger fluid bulk modulus, *e.g.*, $K_f / K_m = 100$. For selected surface parameters, Fig. 10(b) displays the influence of fluid compressibility on the effective Biot modulus while Figs. 10(c, d) illustrate how residual surface stress and surface moduli influence the effective Biot modulus.

4.3 Mechanical response of fluid-saturated porous material with surface effects under uniaxial/multiaxial stretching

The proposed cuboidal model is next applied to describe the mechanical response of an isotropic fluid-saturated porous material in either undrained or drained state. For these two limiting cases, there is no fluid flow and hence the mechanical response may be taken as linear elastic.

For illustration, consider first the case of quasi-static uniaxial stretching, $\sigma_x = \sigma$, $\sigma_y = \sigma_z = 0$. The stress versus strain relations for both drained and undrained states can be expressed as:

$$\begin{aligned} \sigma_x &= E_d \varepsilon_x, \\ \sigma_x &= E_u \varepsilon_x. \end{aligned} \tag{62}$$

As shown in Fig. 11(a), for fixed strain, the presence of surface effects enlarges the stress or, equivalently, stiffens the fluid-saturated porous material. Further, at the same strain level, the stress in the undrained state is larger than that in the drained state. This implies that, under loading, the force of the fluid-saturated porous material eventually attenuates when the strain remains fixed, causing the so-called poroelastic relaxation (Hu and Suo, 2012; Wang et al., 2020).

Consider next the case of quasi-static non-proportional stretching, $\sigma_x = \sigma$, $\sigma_y = \sigma_z = 0.5\sigma$. Corresponding stress versus strain relations for drained and undrained states become:

$$\begin{aligned} \sigma_x &= \frac{E_d}{1 - 2\nu_d} \varepsilon_x, \\ \sigma_x &= \frac{E_u}{1 - 2\nu_u} \varepsilon_x. \end{aligned} \tag{63}$$

Again, as shown in Fig. 11(b), for non-proportional stretching, surface effects increase the stress compared to that without surface effects at the same strain, and the stress in the

undrained state is larger than that in the drained state (poroelastic relaxation). Compared with uniaxial stretching (blue lines in Fig. 11(a)), the stress σ_x with non-proportional stretching (blue lines in Fig. 11(b)) is larger for the same strain ε_x. Besides, as the porous material has a zero drained Poisson ratio, non-proportional stretching has no influence on σ_x, *i.e.*, the red lines of Fig. 11(b) coincide with the red lines of Fig. 11(a). In contrast, in the undrained state, the Poisson effect enables a larger stress σ_x with non-proportional stretching relative to that with uniaxial stretching. That is, the variation of fluid volume between undrained and drained states, namely, the difference between the blue line and the corresponding red line, increases with the lateral stretch.

4.4 Stress concentration of small liquid inclusion embedded in fluid-saturated medium with surface effects

As another application, the cuboidal open cell model is employed to describe stress concentration generated by a small liquid inclusion with non-negligible surface tension (e.g., a cell), embedded in a fluid-saturated porous material that contains distributed small pores and hence exhibits surface effects. Due to challenges in mathematically modeling such double influence of surface effects, how such stress concentration is dependent upon surface effects remains elusive, especially when surface effects play a significant role in the deformation and stressing of the porous material surrounding the liquid inclusion.

Built upon our previous work (Ti et al., 2021), consider a compressible spherical liquid inclusion that is surrounded by an infinite, isotropic, fluid-saturated porous material, with surface tension acting on its surface, as shown schematically in Fig. 12(a). Further, it is assumed that the fluid-saturated porous matrix is idealized and can be modeled using the proposed cuboidal open cell model. It should be pointed out that, for the first time, we consider the case when both the liquid inclusion and the matrix exhibit surface effects. To solve this complex problem, we consider again two limiting cases (undrained state and drained state) of the matrix, such that no fluid flow needs to be considered and the mechanical response may be taken as linear elastic.

With uniaxial stretching applied at remote, the stress fields of a spherical liquid inclusion in a poroelastic matrix considering surface effects can be obtained straightforwardly using the theoretical results presented in our previous work (Ti et al., 2021). Specifically, we replace the mechanical parameters of continuum solid matrix considered in our previous study with the effective mechanical properties derived in the present study for fluid-saturated porous matrix.

The results show that stress concentration most likely occurs at point A located on the inclusion-matrix interface in the direction of far-filed stretching; Fig. 12(a). To quantify the stress concentration, the explicit solution for the radial stress component at point A is presented below:

$$\sigma_{rr,A} = 3E_p\left(-1+\nu_p\right)\varepsilon^{\infty}\left\{2\left(19+26\nu_p+7\nu_p^2\right)\left(\frac{\gamma}{E_pR}\right)^2+\left(-7+5\nu_p\right)\frac{K_i}{E_u}\right.$$
$$\left.-\left[22+57\frac{K_i}{E_p}+21\nu_p^2\frac{K_i}{E_p}+6\nu_p\left(5+13\frac{K_i}{E_p}\right)\right]\frac{\gamma}{E_pR}\right\}\Bigg/\left\{\left[-7-17\frac{\gamma}{E_pR}\right.\right. \quad (64)$$
$$\left.\left.+19\nu_p^2\frac{\gamma}{E_pR}+\nu_p\left(5+2\frac{\gamma}{E_pR}\right)\right]\left[-2+2\left(1+\nu_p\right)\frac{\gamma}{E_pR}-3\left(1+\nu_p\right)\frac{K_i}{E_p}\right]\right\},$$

where $E_p = E_d$ (or E_u) and $\nu_p = \nu_d$ (or ν_u) are the Young's modulus and Poisson ratio of the porous matrix material in drained (undrained) state, analytically estimated in Section 3.3 of this study, ε^{∞} is the strain of far field, γ is the surface tension, R is the radius of liquid inclusion, and K_i is the bulk modulus of liquid inclusion. When surface tension of the liquid inclusion is negligible, the present results are consistent with existing results (Chen et al., 2018).

Based on the result of (65), we show in Figs. 12(b) and (c) how surface effects can influence the stress concentration of the small liquid inclusion in terms of radial stress $\sigma_{rr,A}$ at point A. For the plotting, surface tension at inclusion-matrix interface is taken as $\gamma = 0.1E_mR$ while surface moduli and residual surface stress in the matrix are systematically varied, with the remaining parameters fixed at $K_i = 0.1K_m$, $\nu_m = 0.3$ and $\phi = 0.8$. We observe that the stress concentration (*i.e.*, radial stress $\sigma_{rr,A}$ at point A) monotonically increases as either residual surface stress or surface moduli of the fluid-saturated porous matrix are increased; Figs. 12(b) and (c). Besides, the stress concentration decreases significantly from undrained state to drained state due to fluid flow of the porous matrix, which means the presence of fluid enhances stress concentration around the inclusion.

5. Discussion

The poroelastic behaviors of a porous material saturated with compressible fluid can be affected significantly by surface effects, especially if its porous network of solid ligaments is

soft. According to our previous work (Chen et al., 2021), due to the surface effects induced by interaction between fluid and solid skeleton, hydrogel can exhibit swelling and snap-though instability (Cai and Suo, 2011; Hong et al., 2009; Hong et al., 2008). Therefore, for a fluid-saturated porous material with large surface parameters (or small elastic moduli), surface effects play a significant role in its mechanical behavior. To help understand the extent to which surface effects influence the mechanical behavior, Fig. 13 displays dimensionless residual stresses (*i.e.*, surface tension) and porosities for common porous materials. (It should be noticed that, due to lack of available test data, the surface stresses shown in Fig. 13 are for the fluid and vapor, but in the current study they are for the fluid and solid).

In our previous studies (Chen et al., 2021; Ti et al., 2022), the dependence of effective poroelastic parameters upon surface effects was quantified theoretically for two common microstructures: liquid inclusions and macromolecular network. In the current study, we provide another microstructure (*i.e.*, open-celled cellular structure) for mechanical analysis. It is therefore of interest to compare theoretical models developed for different microstructures exhibiting surface effects. For the macromolecular network model, the macromolecular chains are assumed to be free and random, so that the model is valid when the porosity is close to 100% (typically > 99%). On the contrary, the liquid inclusions model is applicable for porous materials with relatively low porosities (typically < 70%) or closed pores. The proposed cuboidal model fills the gap of the two microstructures, *i.e.*, it can be used to calculate the effective poroelastic parameters of fluid-saturated porous materials when the other two models are not applicable.

The cuboidal open cell model can be extended to cover a wide variety of pore morphologies, such as tetrahedron, hexagonal prism, pentagonal dodecahedron and tetrakaidekahedron (Gibson and Ashby, 1997). Nonetheless, among the different pore morphologies considered, the cuboidal model is the simplest and can accurately describe the main features of the poroelasticity problem, *i.e.*, deformation of stretching/bending ligaments, and explore physical mechanisms underlying the influence of surface effects on the poroelastic parameters of fluid-saturated porous materials with small pores. In addition, the model can be used to not only study the viscous-poroelastic and dynamical behaviors of fluid-saturated porous materials with surface effects, but also analyze cross-disciplinary problems such as thermo-solid-fluidic coupling and acoustic-solid-fluidic coupling. However, it must be emphasized that, in practice, many poroelastic materials are soft and largely deformable and hence it is necessary to extend the present theoretical model to analyze the role played by surface effect in the large deformation of soft poroelastic materials. To this end, the cuboidal model depicted in Fig. 1 may be linked to the theory developed previously to quantify surface effects on large deflection of elastic nanobeam (*e.g.*, (Liu et al., 2016a; Zeng and Zheng, 2010)). Besides, as these soft materials often exhibit viscoelastic behaviors due to say

entangled chains (Liu et al., 2019), viscoelasticity should also be considered in addition to large deformation.

Lastly but not lest importantly, it should be noted that extending our model to fluid-saturated biological systems requires squarely addressing challenging issues such as solvent flow and charge. For typical instance, in addition to filament system, the protein content, charged molecules (*e.g.*, vimentin and actin), and solvent flow cannot be ignored in cytoplasm (Blüher et al., 2004). Besides, collagen is packed so tightly in hierarchical structures like tendon that the flow of interstitial fluid is heavily restricted (O'brien, 1997). Further, interface properties (*e.g.*, residual surface stress and surface moduli) are dependent upon temperature (Kezwon and Wojciechowski, 2014). Therefore, for complex biological systems, substantial additional justification is needed to extend the current model, with the effects of solvent flow, charge and other factors duly accounted for.

6. Conclusion

A micromechanics model of cuboidal open cell has been proposed to analyze how surface stresses and fluid compressibility affect the effective poroelastic parameters of fluid-saturated porous elastic materials. Together with our Biot-type phenomenological constitutive model developed in an earlier study (Chen et al., 2021), an integrated bottom-up and top-down approach is developed to analyze stress versus strain responses of the porous material subjected to multiaxial loading as well as stress concentration of a liquid inclusion embedded in porous materials. Main conclusions drawn are:

(1) Effective poroelastic moduli for orthotropic, transverse isotropic, and isotropic porous materials saturated with fluid are derived, and the influence of both fluid compressibility and surface stresses on these poroelastic parameters is quantified.

(2) The effects of two different surface parameters - residual surface stress and surface moduli - are coupled: the former dominates the deformation of a bending beam, while the latter dominates the deformation of a stretching beam and has little influence on a bending beam.

(3) The influence of surface stresses on undrained moduli is significant when the bulk modulus of fluid is small, but negligible if the fluid is nearly incompressible.

(4) Key parameters characterizing solid-fluid coupling, *i.e.*, the Biot modulus and the Biot coefficient of effective stress, are determined for isotropic porous materials.

(5) The proposed model is applied to calculate stress versus strain responses of the porous material in both undrained and drained states. Under either uniaxial tension or non-proportional multiaxial tension, surface effects increase the stress compared to that without surface effects at the same strain, and the stress in the undrained state is larger than that in the drained state (poroelastic relaxation).

(6) The model is also applied to demonstrate that the stress concentration of a small liquid inclusion with non-negligible surface tension embedded in a fluid-saturated porous material with surface effects increases as either residual surface stress or surface moduli of the material are increased.

The model developed in this study lays a solid theoretical foundation for exploring how surface effects influence the effective poroelastic parameters of a fluid-saturated porous material as well as its mechanical response when subjected to multiaxial external loadings.

Author statement

Fei Ti: Methodology, Formal analysis, Writing - Original Draft Xin Chen: Methodology, Supervision Writing - Original Draft Moxiao Li: Visualization Writing - Review & Editing Shaobao Liu: Visualization Writing - Review & Editing Tian Jian Lu: Supervision Writing - Review & Editing Funding acquisition

Declaration of interests

The authors declare that they have no known competing financial interests or personal relationships that could have appeared to influence the work reported in this paper.

Acknowledgements

This work was supported by the National Natural Science Foundation of China (12032010, 11902155, 12202348), by the Natural Science Foundation of Jiangsu Province (BK20190382), by the Research Fund of State Key Laboratory of Mechanics and Control of Mechanical Structures (Grant No. MCMS-I-0222K01), by the Fund of Prospective Layout of Scientific Research for NUAA, and by the Foundation for the Priority Academic Program Development of Jiangsu Higher Education Institutions.

References

Ambrosi, D., Ateshian, G.A., Arruda, E.M., Cowin, S., Dumais, J., Goriely, A., Holzapfel, G.A., Humphrey, J.D., Kemkemer, R., Kuhl, E., 2011. Perspectives on biological growth and remodeling. J. Mech. Phys. Solids 59, 863-883.

Ansari, R., Mohammadi, V., Shojaei, M.F., Gholami, R., Sahmani, S., 2014. Postbuckling analysis of Timoshenko nanobeams including surface stress effect. Int. J. Eng. Sci. 75, 1-10.

Baker, S.R., Banerjee, S., Bonin, K., Guthold, M., 2016. Determining the mechanical properties of electrospun poly-ε-caprolactone (PCL) nanofibers using AFM and a novel fiber anchoring technique. Mater. Sci. Eng. C 59, 203-212.

Bennis, H., Benslimane, R., Vicini, S., Mairani, A., Princi, E., 2010. Fibre width measurement and quantification of filler size distribution in paper-based materials by SEM and image analysis. J. Electron Microsc. 59, 91-102.

Biot, M.A., 1941. General Theory of Three dimensional Consolidation. J. Appl. Phys. 12, 155-164.

Biot, M.A., Willis, D., 1957. The elastic coefficients of the theory of consolidation. J. Appl. Mech. 24, 594-601.

Bischoff, J., Arruda, E., Grosh, K., 2002. A microstructurally based orthotropic hyperelastic constitutive law. J. Appl. Mech. 69, 570-579.

Blüher, M., Wilson-Fritch, L., Leszyk, J., Laustsen, P.G., Corvera, S., Kahn, C.R., 2004. Role of insulin action and cell size on protein expression patterns in adipocytes. J. Biol. Chem. 279, 31902-31909.

Cai, S., Suo, Z., 2011. Mechanics and chemical thermodynamics of phase transition in temperature-sensitive hydrogels. J. Mech. Phys. Solids 59, 2259-2278.

Champion, Y., Laurent-Brocq, M., Lhuissier, P., Charlot, F., Moreira Jorge Junior, A., Barsuk, D., 2019. Understanding the Interdependence of Penetration Depth and Deformation on Nanoindentation of Nanoporous Silver. Metals 9, 1346.

Chen, X., Li, M., Liu, S., He, W., Ti, F., Dong, Y., Genin, G.M., Xu, F., Lu, T.J., 2020. Mechanics tuning of liquid inclusions via bio-coating. Extreme Mech. Lett., 101049.

Chen, X., Li, M., Yang, M., Liu, S., Genin, G.M., Xu, F., Lu, T.J., 2018. The elastic fields of a compressible liquid inclusion. Extreme Mech. Lett. 22, 122-130.

Chen, X., Ti, F., Li, M., Liu, S., Lu, T.J., 2021. Theory of fluid saturated porous media with surface effects. J. Mech. Phys. Solids 151, 104392.

Cheng, A.-D., 1997. Material coefficients of anisotropic poroelasticity. Int. J. Rock Mech. Min. Sci. 34, 199-205.

Cheng, A.-D., Abousleiman, Y., Roegiers, J.-C., 1993. Review of some poroelastic effects in rock mechanics. Int. J. Rock Mech. Min. Sci. Geomech. Abstr. 30, 1119-1126.

Coussy, Dormieux, Detournay, 1998. From mixture theory to biot's approach for porous media. Int. J. Solids Struct. 35, 4619-4635.

Deck, M.D., Henschke, C., Lee, B.C., Zimmerman, R.D., Hyman, R.A., Edwards, J., Saint Louis, L.A., Cahill, P.T., Stein, H., Whalen, J.P., 1989. Computed tomography versus magnetic resonance imaging of the brain a collaborative interinstitutional study. Clin. Imaging 13, 2-15.

Detournay, E., Cheng, A.H.-D., 1993. Fundamentals of poroelasticity, Comprehensive Rock Engineering: Principles, Practice and Projects. Pergamon Press, Oxford, pp. 113-171.

Dey, A., Mukhopadhyay, A.K., Gangadharan, S., Sinha, M.K., Basu, D., 2009. Weibull modulus of nano-hardness and elastic modulus of hydroxyapatite coating. J. Mater. Sci. 44, 4911-4918.

Digby, P., 1981. The effective elastic moduli of porous granular rocks. J. Appl. Mech. 48, 803-808.

Dormieux, L., Kondo, D., Ulm, F.-J., 2006. Microporomechanics. John Wiley & Sons.

Du, J., Liu, J., Yao, S., Mao, H., Peng, J., Sun, X., Cao, Z., Yang, Y., Xiao, B., Wang, Y., 2017. Prompt peripheral nerve regeneration induced by a hierarchically aligned fibrin nanofiber hydrogel. Acta Biomater. 55, 296-309.

Dupère, I.D., Lu, T.J., Dowling, A.P., 2005. Acoustic properties, Cellular Ceramics: Structure, Manufacturing, Properties and Applications. WILEY-VCH, Weinheim, pp. 381-399.

Eichhorn, S., Sirichaisit, J., Young, R., 2001. Deformation mechanisms in cellulose fibres, paper and wood. J. Mater. Sci. 36, 3129-3135.

Eshelby, J., 1959. The elastic field outside an ellipsoidal inclusion. Proc. Roy. Soc. London A 252, 561-569.

Eshelby, J.D., 1957. The determination of the elastic field of an ellipsoidal inclusion, and related problems. Proc. Roy. Soc. London A 241, 376-396.

Feng, X.-Q., Xia, R., Li, X., Li, B., 2009. Surface effects on the elastic modulus of nanoporous materials. Appl. Phys. Lett. 94, 011916.

Flory, P.J., 1942. Thermodynamics of high polymer solutions. J. Chem. Phys. 10, 51-61.

Flory, P.J., 1953. Principles of polymer chemistry. Cornell university press, Ithaca, NY.

Flory, P.J., Rehner Jr, J., 1943. Statistical mechanics of cross-linked polymer networks I. Rubberlike elasticity. J. Chem. Phys. 11, 512-520.

Gibson, I., Ashby, M.F., 1982. The mechanics of three-dimensional cellular materials. Proc. Roy. Soc. London A 382, 43-59.

Gibson, L., 1985. The mechanical behaviour of cancellous bone. J. Biomech. 18, 317-328.

Gibson, L.J., Ashby, M.F., 1997. Cellular solids: structure and properties, 2nd ed. Cambridge university press, Cambridge.

Green, D., Wang, H., 1990. Specific storage as a poroelastic coefficient. Water Resour. Res. 26, 1631-1637.

Gurtin, M.E., Murdoch, A.I., 1975. A continuum theory of elastic material surfaces. Arch. Ration. Mech. An. 57, 291-323.

Gurtin, M.E., Murdoch, A.I., 1978. Surface stress in solids. Int. J. Solids Struct. 14, 431-440.

Hauner, I.M., Deblais, A., Beattie, J.K., Kellay, H., Bonn, D., 2017. The dynamic surface tension of water. J. Phys. Chem. Lett. 8, 1599-1603.

He, J., Lilley, C.M., 2008. Surface effect on the elastic behavior of static bending nanowires. Nano Lett. 8, 1798-1802.

Hedayati, R., Sadighi, M., Mohammadi-Aghdam, M., Hosseini-Toudeshky, H., 2018. Comparison of elastic properties of open-cell metallic biomaterials with different unit cell types. J. Biomed. Mater. Res. B 106, 386-398.

Hertz, H., 1882. Über die Berührung fester elastischer Körper. J. Reine Angew. Math. 92, 22.

Hicsasmaz, Z., Clayton, J., 1992. Characterization of the pore structure of starch based food materials. Food Struct. 11, 115-132.

Hill, R., 1965. A self-consistent mechanics of composite materials. J. Mech. Phys. Solids 13, 213-222.

Hong, W., Liu, Z., Suo, Z., 2009. Inhomogeneous swelling of a gel in equilibrium with a solvent and mechanical load. Int. J. Solids Struct. 46, 3282-3289.

Hong, W., Zhao, X., Zhou, J., Suo, Z., 2008. A theory of coupled diffusion and large deformation in polymeric gels. J. Mech. Phys. Solids 56, 1779-1793.

Hu, J., Wang, S., Wang, L., Li, F., Pingguan-Murphy, B., Lu, T.J., Xu, F., 2014. Advances in paper-based point-of-care diagnostics. Biosens. Bioelectron. 54, 585-597.

Hu, Y., Suo, Z., 2012. Viscoelasticity and poroelasticity in elastomeric gels. Acta Mech. Solida Sin. 25, 441-458.

Huggins, M.L., 1941. Solutions of long chain compounds. J. Chem. Phys. 9, 440-440.

Hutchinson, J., 2001. Shear coefficients for Timoshenko beam theory. J. Appl. Mech. 68, 87-92.

Jha, A., Tripathy, P.P., 2020. Influence of solar drying and storage conditions on microstructure, crack propagation and nano-hardness of paddy and wheat. J. Cereal Sci. 95, 103054.

Jin, S.E., Bae, J.W., Hong, S., 2010. Multiscale observation of biological interactions of nanocarriers: From nano to macro. Microsc. Res. Tech. 73, 813-823.

Kar, T., Patra, N., 2020. Pyrene-based fluorescent supramolecular hydrogel: scaffold for nanoparticle synthesis. J. Phys. Org. Chem. 33, e4026.

Kendall, K., Alford, N.M., Birchall, J.D., 1987. Elasticity of particle assemblies as a measure of the surface energy of solids. Proc. Roy. Soc. London A 412, 269-283.

Kezwon, A., Wojciechowski, K., 2014. Effect of temperature on surface tension and surface dilational rheology of type I collagen. Colloids Surf. Physicochem. Eng. Aspects 460, 168-175.

Khalili, N., Geiser, F., Blight, G., 2004. Effective stress in unsaturated soils: Review with new evidence. Int. J. Geomech. 4, 115-126.

Krichen, S., Liu, L., Sharma, P., 2019. Liquid inclusions in soft materials: Capillary effect, mechanical stiffening and enhanced electromechanical response. J. Mech. Phys. Solids 127, 332-357.

Lakes, R., 1993. Materials with structural hierarchy. Nature 361, 511-515.

Li, K., Gao, X.-L., Subhash, G., 2006. Effects of cell shape and strut cross-sectional area variations on the elastic properties of three-dimensional open-cell foams. J. Mech. Phys. Solids 54, 783-806.

Liu, C., Rajapakse, R., 2009. Continuum models incorporating surface energy for static and dynamic response of nanoscale beams. IEEE T. Nanotechnol. 9, 422-431.

Liu, H., Han, Y., Yang, J.-L., 2016a. Surface effects on large deflection of a curved elastic nanobeam under static bending. Int. J. Appl. Mech. 8, 1650098.

Liu, H., Holzapfel, G.A., Skallerud, B.H., Prot, V., 2019. Anisotropic finite strain viscoelasticity: Constitutive modeling and finite element implementation. J. Mech. Phys. Solids 124, 172-188.

Liu, L.-Z., Ye, X.-L., Jin, H.-J., 2016b. Interpreting anomalous low-strength and low-stiffness of nanoporous gold: Quantification of network connectivity. Acta Mater. 118, 77-87.

Lopes, M.A., Monteiro, F., Santos, J., Serro, A., Saramago, B., 1999. Hydrophobicity, surface tension, and zeta potential measurements of glass-reinforced hydroxyapatite composites. J. Biomed. Mater. Res. 45, 370-375.

Lu, P., He, L., Lee, H., Lu, C., 2006. Thin plate theory including surface effects. Int. J. Solids Struct. 43, 4631-4647.

Lu, T., Stone, H.A., Ashby, M., 1998. Heat transfer in open-cell metal foams. Acta Mater. 46, 3619-3635.

Lu, T.J., Xu, F., Wen, T., 2013. Thermo-fluid behaviour of periodic cellular metals. Science Press Beijing, and Springer-Verlag Berlin Heidelberg.

Mathias, S.A., Nielsen, S., Ward, R.L., 2019. Storage coefficients and permeability functions for coal-bed methane production under uniaxial strain conditions. Transp. Porous Media 130, 627-636.

Mindlin, R.D., 1949. Compliance of elastic bodies in contact. J. Appl. Mech. 16, 259-268.

Nix, W.D., Gao, H., 1998. An atomistic interpretation of interface stress. Scripta Mater. 39, 1653-1661.

O'brien, M., 1997. Structure and metabolism of tendons. Scand. J. Med. Sci. Sports 7, 55-61.

O'Shea, D.J., Attard, M.M., Kellermann, D.C., 2019. Hyperelastic constitutive modelling for transversely isotropic composites and orthotropic biological tissues. Int. J. Solids Struct. 169, 1-20.

Oikonomopoulou, V.P., Krokida, M.K., Karathanos, V.T., 2011. Structural properties of freeze-dried rice. J. Food Eng. 107, 326-333.

Rice, J.R., Cleary, M.P., 1976. Some basic stress diffusion solutions for fluid-saturated elastic porous media with compressible constituents. Rev. Geophys. 14, 227-241.

Sahi, S., 2003. The interfacial properties of the aqueous phases of full recipe bread doughs. J. Cereal Sci. 37, 205-214.

Scanlon, M., Zghal, M., 2001. Bread properties and crumb structure. Food Res. Int. 34, 841-864.

Seok, J.Y., Lee, J., Yang, M., 2018. Self-generated nanoporous silver framework for high-performance iron oxide pseudocapacitor anodes. ACS Appl. Mater. Interfaces 10, 17223-17231.

Shenoy, V.B., 2005. Atomistic calculations of elastic properties of metallic fcc crystal surfaces. Phys. Rev. B 71, 094104.

Silva, M., Cyster, L., Barry, J., Yang, X., Oreffo, R., Grant, D., Scotchford, C., Howdle, S., Shakesheff, K., Rose, F., 2006. The effect of anisotropic architecture on cell and tissue infiltration into tissue engineering scaffolds. Biomaterials 27, 5909-5917.

Skempton, A., 1954. The pore-pressure coefficients A and B. Geotechnique 4, 143-147.

Style, R.W., Jagota, A., Hui, C.Y., Dufresne, E.R., 2017. Elastocapillarity: Surface tension and the mechanics of soft solids. Annu. Rev. Condens. Matter Phys. 8, 99-118.

Su, L., Wang, M., Yin, J., Ti, F., Yang, J., Ma, C., Liu, S., Lu, T.J., 2022. Distinguishing poroelasticity and viscoelasticity of brain tissue with time scale. Acta Biomater., in press.

Tanpichai, S., Witayakran, S., Srimarut, Y., Woraprayote, W., Malila, Y., 2019. Porosity, density and mechanical properties of the paper of steam exploded bamboo microfibers controlled by nanofibrillated cellulose. J. Mater. Res. Technol. 8, 3612-3622.

Thornton, C., 1993. On the relationship between the modulus of particulate media and the surface energy of the constituent particles. J. Phys. D: Appl. Phys. 26, 1587.

Ti, F., Chen, X., Li, M., Sun, X., Liu, S., Lu, T.J., 2022. Cylindrical compressible liquid inclusion with surface effects. J. Mech. Phys. Solids, 104813.

Ti, F., Chen, X., Yang, H., Liu, S., Lu, T.J., 2021. A theory of mechanobiological sensation: strain amplification/attenuation of coated liquid inclusion with surface tension. Acta Mech. Sin. 37, 145-155.

Walton, K., 1978. The oblique compression of two elastic spheres. J. Mech. Phys. Solids 26, 139-150.

Walton, K., 1987. The effective elastic moduli of a random packing of spheres. J. Mech. Phys. Solids 35, 213-226.

Wang, G.-F., Feng, X.-Q., 2009. Timoshenko beam model for buckling and vibration of nanowires with surface effects. J. Phys. D: Appl. Phys. 42, 155411.

Wang, J., Huang, Z., Duan, H., Yu, S., Feng, X., Wang, G., Zhang, W., Wang, T., 2011. Surface stress effect in mechanics of nanostructured materials. Acta Mech. Solida Sin. 24, 52-82.

Wang, M., Liu, S., Xu, Z., Qu, K., Li, M., Chen, X., Xue, Q., Genin, G.M., Lu, T.J., Xu, F., 2020. Characterizing poroelasticity of biological tissues by spherical indentation: An improved theory for large relaxation. J. Mech. Phys. Solids, 103920.

Westerlind, B.S., Berg, J.C., 1988. Surface energy of untreated and surface-modified cellulose fibers. J. Appl. Polym. Sci. 36, 523-534.

Xia, R., Feng, X.-Q., Wang, G.-F., 2011a. Effective elastic properties of nanoporous materials with hierarchical structure. Acta Mater. 59, 6801-6808.

Xia, R., Li, X., Qin, Q., Liu, J., Feng, X.-Q., 2011b. Surface effects on the mechanical properties of nanoporous materials. Nanotechnology 22, 265714.

Ye, X.-L., Liu, L.-Z., Jin, H.-J., 2016. Responsive nanoporous metals: recoverable modulations on strength and shape by watering. Nanotechnology 27, 325501.

Yoon, B.H., Koh, Y.H., Park, C.S., Kim, H.E., 2007. Generation of large pore channels for bone tissue engineering using camphene-based freeze casting. J. Am. Ceram. Soc. 90, 1744-1752.

Zeng, D., Zheng, Q., 2010. Large deflection theory of nanobeams. Acta Mech. Solida Sin. 23, 394-399.

Table 1. Relevant p**arameters for common porous materials**

	Residual surface stress (N/m)	Ligament size	Young's modulus of solid	Porosity (%)
Nanoporous gold	1.41 (Shenoy, 2005)	38-48 nm (Liu et al., 2016b)	79 GPa (Liu et al., 2016b)	65-75 (Liu et al., 2016b)
Nanoporous sliver	0.89 (Shenoy, 2005)	50-350 nm (Seok et al., 2018)	73.5-78.5 GPa (Champion et al., 2019)	35-65 (Seok et al., 2018)
Aligned fibrin nanofiber hydrogel (AFG)	0.051-0.066 (Kar and Patra, 2020)	100 nm (Du et al., 2017)	17-89 MPa (Baker et al., 2016)	98.5 (Du et al., 2017)
Bread	0.028-0.04 (Sahi, 2003)	6-200 μm (Hicsasmaz and Clayton, 1992)	132-851 kPa (Scanlon and Zghal, 2001)	88-93 (Scanlon and Zghal, 2001)
Rice	0.072 (Hauner et al., 2017)	10-50μm (Oikonomopoulou et al., 2011)	0.15-0.41 GPa (Jha and Tripathy, 2020)	40-50 (Oikonomopoulou et al., 2011)
Porous HA scaffolds	0.047 (Lopes et al., 1999)	10μm (Yoon et al., 2007)	63-100 GPa (Dey et al., 2009)	76 (Yoon et al., 2007)
Paper	0.064-0.073 (Westerlind and Berg, 1988)	10-50 μm (Bennis et al., 2010)	8.9-47.7 GPa (Eichhorn et al., 2001)	57.1-73.6 (Tanpichai et al., 2019)

Table 2. Relations among poroelastic parameters for isotropic fluid-saturated porous materials

	K_d, G, H, R	K_u, G, α, B	K_d, G, α, M	K_u, K_d, G, α
K_d	K_d	$K_u(1-\alpha B)$	K_d	K_d
ν	$\frac{3K_d-2G}{2(3K_d+G)}$	$\frac{3K_u(1-\alpha B)-2G}{2[3K_u(1-\alpha B)+G]}$	$\frac{3K_d-2G}{2(3K_d+G)}$	$\frac{3K_d-2G}{2(3K_d+G)}$
H	H	$K_u\left(\frac{1}{\alpha}-B\right)$	$\frac{K_d}{\alpha}$	$\frac{K_d}{\alpha}$
R	R	$K_u B\left(\frac{1}{\alpha}-B\right)$	$\frac{MK_d}{K_d+M\alpha^2}$	$\frac{K_d(K_u-K_d)}{\alpha^2 K_u}$
K_u	$\frac{KH^2}{H^2-KR}$	K_u	$M\alpha^2+K_d$	K_u
ν_u	$\frac{3K_dH^2-2G(H^2-K_dR)}{6K_dH^2+2G(H^2-K_dR)}$	$\frac{3K_u-2G}{2(3K_u+G)}$	$\frac{3(K_d+M\alpha^2)-2G}{6(K_d+M\alpha^2)+2G}$	$\frac{3K_u-2G}{2(3K_u+G)}$
α	$\frac{K_d}{H}$	α	α	α
M	$\frac{RH^2}{H^2-K_dR}$	$\frac{K_uB}{\alpha}$	M	$\frac{K_u-K_d}{\alpha^2}$
B	$\frac{R}{H}$	B	$\frac{\alpha M}{K_d+M\alpha^2}$	$\frac{K_u-K_d}{\alpha K_u}$
η	$\frac{3GK_d}{(4G+3K_d)H}$	$\frac{3\alpha G}{4G+3K_u(1-\alpha B)}$	$\frac{3\alpha G}{4G+3K_d}$	$\frac{3\alpha G}{4G+3K_d}$
S	$\frac{1}{R}-\frac{4GK_d}{(4G+3K_d)H^2}$	$\frac{\alpha(4G+3K_u)}{[4G+3K_u(1-\alpha B)]BK_u}$	$\frac{4K_d+3(K_d+M\alpha^2)}{(4G+3K_d)M}$	$\frac{\alpha^2(4G+3K_u)}{(4G+3K_d)(K_u-K_d)}$
C	$\frac{\alpha H}{K_dR}$	$\frac{\alpha}{K_u(1-\alpha B)B}$	$\frac{K_d+M\alpha^2}{K_dM}$	$\frac{\alpha^2K_u}{K_d(K_u-K_d)}$

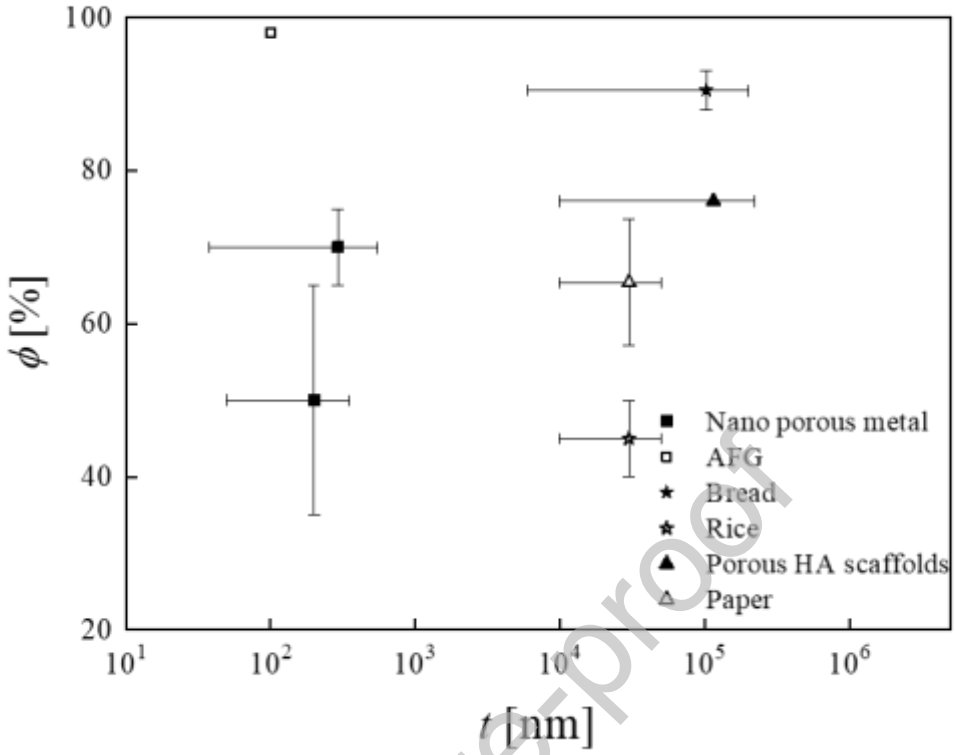

Figure 1. Ligament sizes and porosities of representative fluid-saturated porous media.

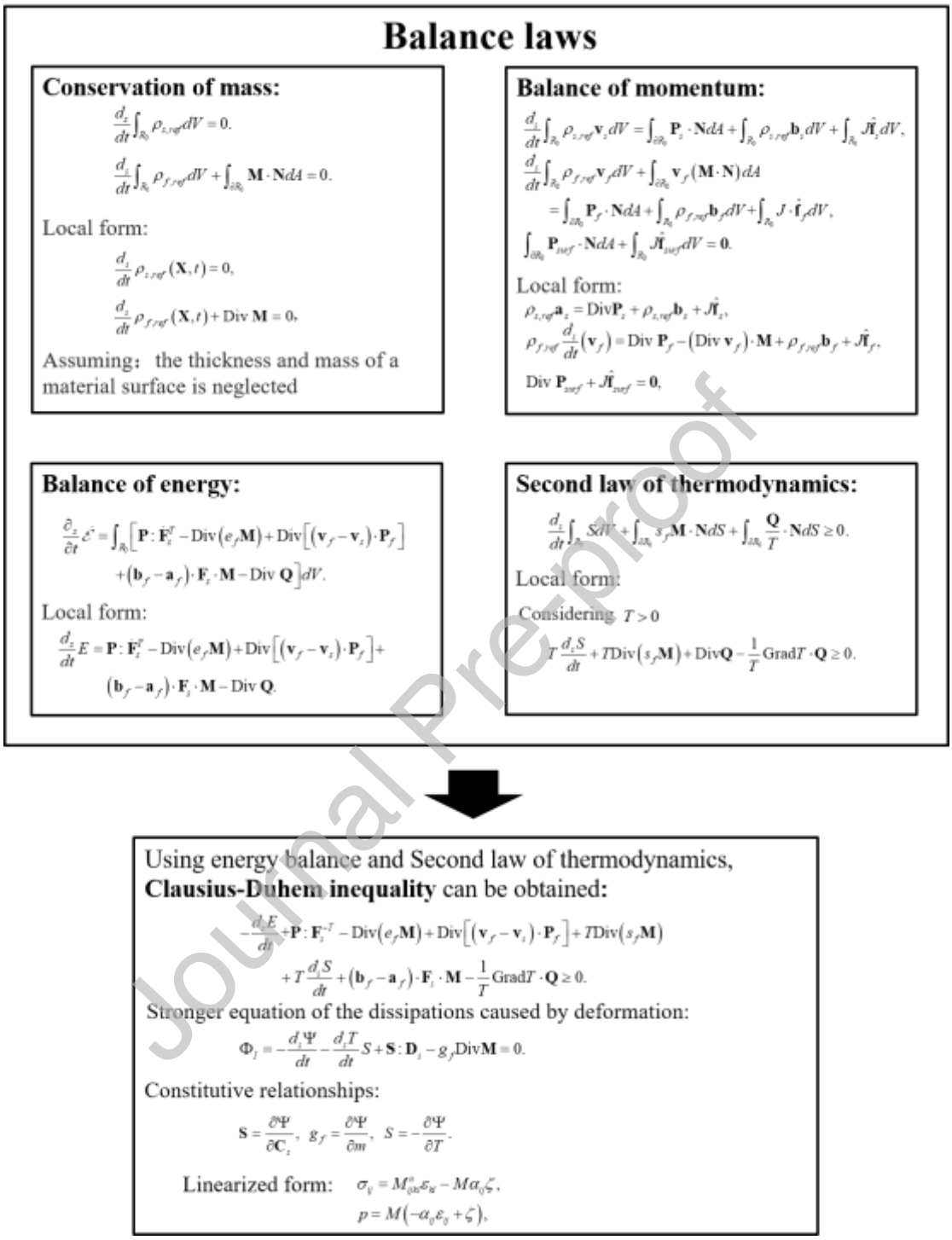

Figure 2. Theoretical framework of constitutive modeling for fluid-saturated porous media with surface effects (Chen et al., 2021).

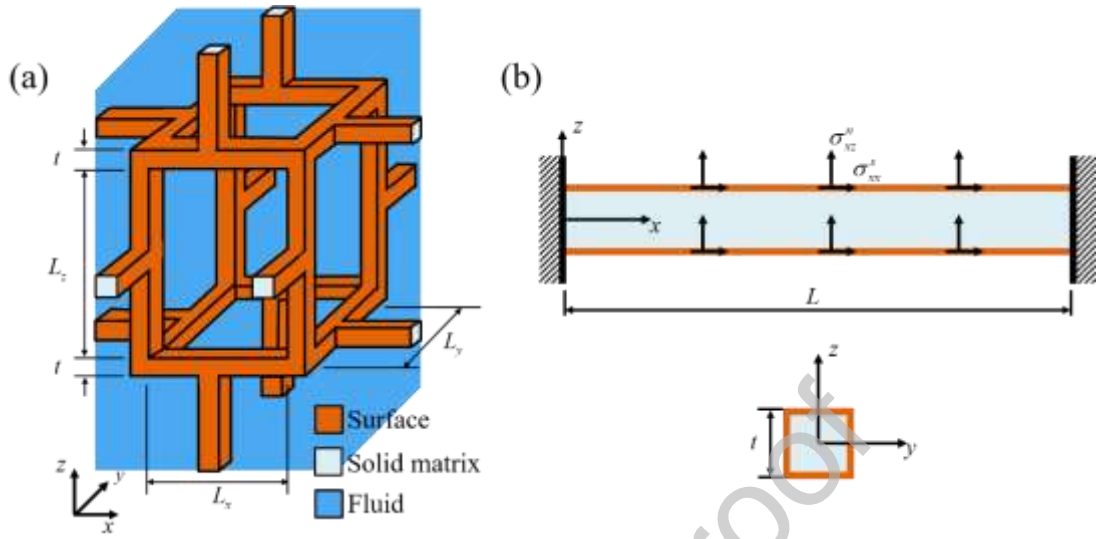

Figure 3. Schematic diagram. (a) Unit cell model for fluid-saturated porous materials with open cells. (b) Timoshenko beam model with surface effects.

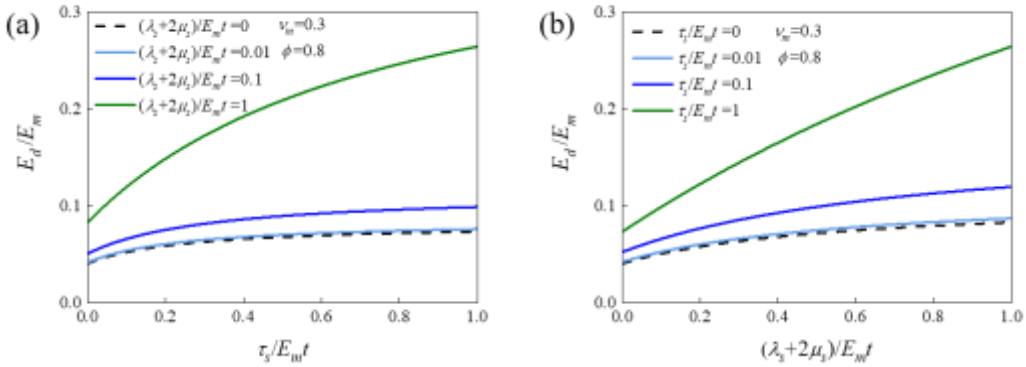

Figure 4. Influence of surface parameters on the effective drained Young's modulus. (a) Influence of residual surface stress. The effective drained Young's modulus increases with the increase of residual surface stress. (b) Influence of surface moduli, with different colors representing different residual surface stresses. The effective drained Young's modulus increases with the increase of surface moduli. The two surface parameters have a coupling effect: the larger the surface moduli, the greater the influence of residual surface stress; and the larger the residual surface stress, the greater the influence of surface moduli. For the plotting, $\nu_m = 0.3$ and $\phi = 0.8$ are selected.

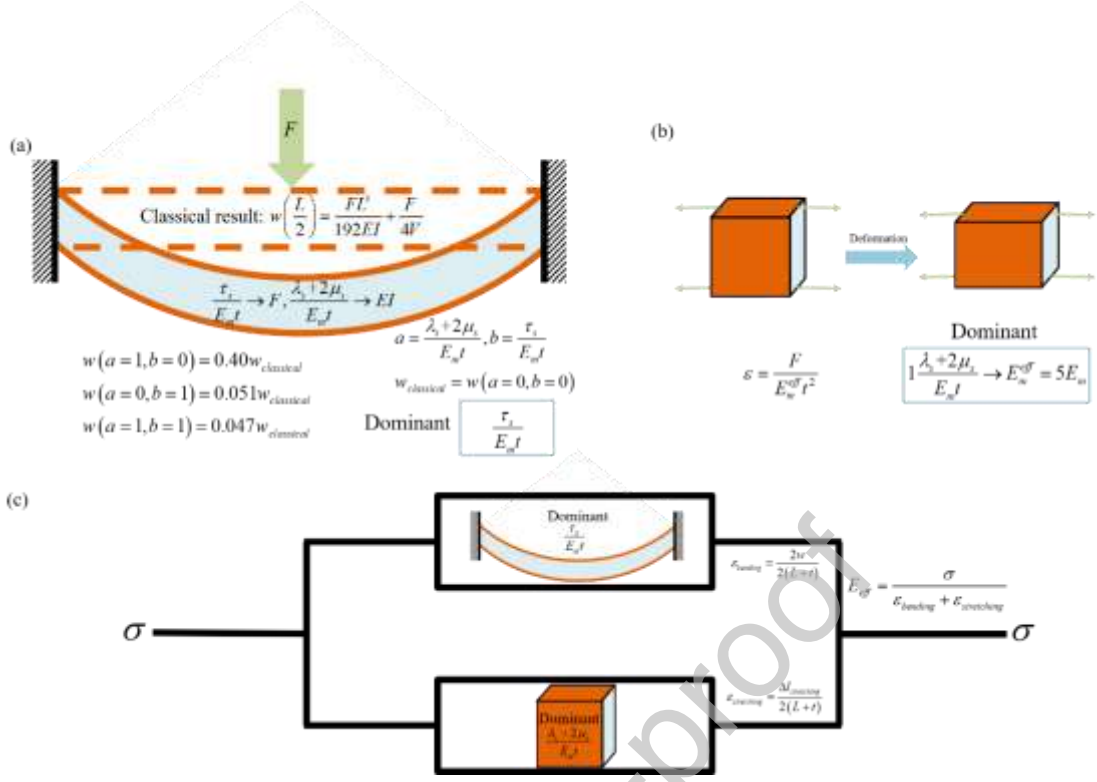

Figure 5. Schematic diagram of the Timoshenko beam under loading. (a) Timoshenko beam under bending. According to the governing equations (Liu and Rajapakse, 2009), the residual surface stress can be considered as a deformation induced distributed force opposite to the concentrated load at the middle of the beam, and the surface moduli can be considered as a film with no thickness which can increase the bending stiffness of the beam *EI*. It can be seen from the classical results that when two surface parameters of the same magnitude, the residual surface stress has a greater impact on deformation than the surface moduli. Therefore, residual surface stress dominates for the bending beam. (b) Beam under tensile force. The beam with surface effects can be considered as to be covered by a film, which increases the Young's modulus of the beam. And the residual surface stress has no influence on the deformation. Therefore, surface moduli dominate for the bending beam. (c) Schematic diagram of coupling effect. The strain of the unit cell model for the porous media consist of two parts: deflection of the bending beam and strain of the stretched beam. The beam displacement, surface parameter, and external load exhibit relationships similar to those among the current, electrical resistance and voltage in electricity.

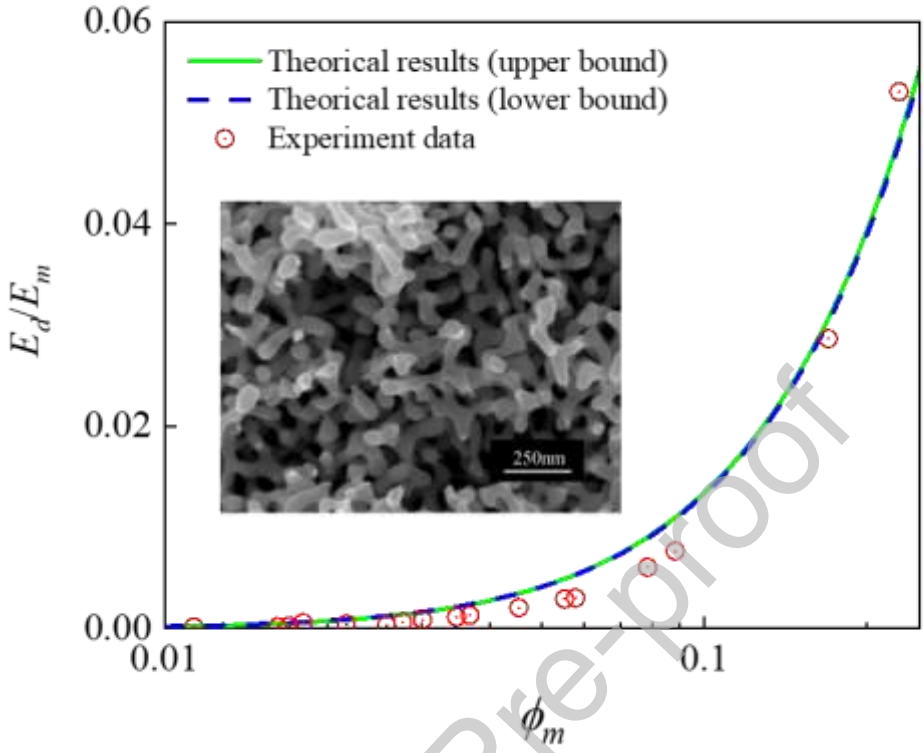

Figure 6. Influence of volume fraction of solid on effective drained Young's modulus (normalized by the modulus of solid matrix) for nanoporous gold. The experiment data and SEM image of nanoporous gold are from a previous study (Liu et al., 2016b). Nanoporous gold samples with different ligament sizes exhibit different effective porosities. For nanoporous materials under drained state, the effective mechanical parameters depend on the volume fraction of solid matrix ϕ_m and two dimensionless surface parameters $\left(\lambda_s+2\mu_s\right)/E_m t$ and $\tau_s/E_m t$. Given that nanoporous samples with different porosities have different ligament sizes *t*, the dimensionless surface parameters are different. Therefore, the upper and lower bounds of $\left(\lambda_s+2\mu_s\right)/E_m t$ and $\tau_s/E_m t$ used in theoretical modeling. The theoretical results fit well with experimental results and, due to the high stiffness of gold relative to water, surface effects have little influence the effective poroelastic parameters of nanoporous gold.

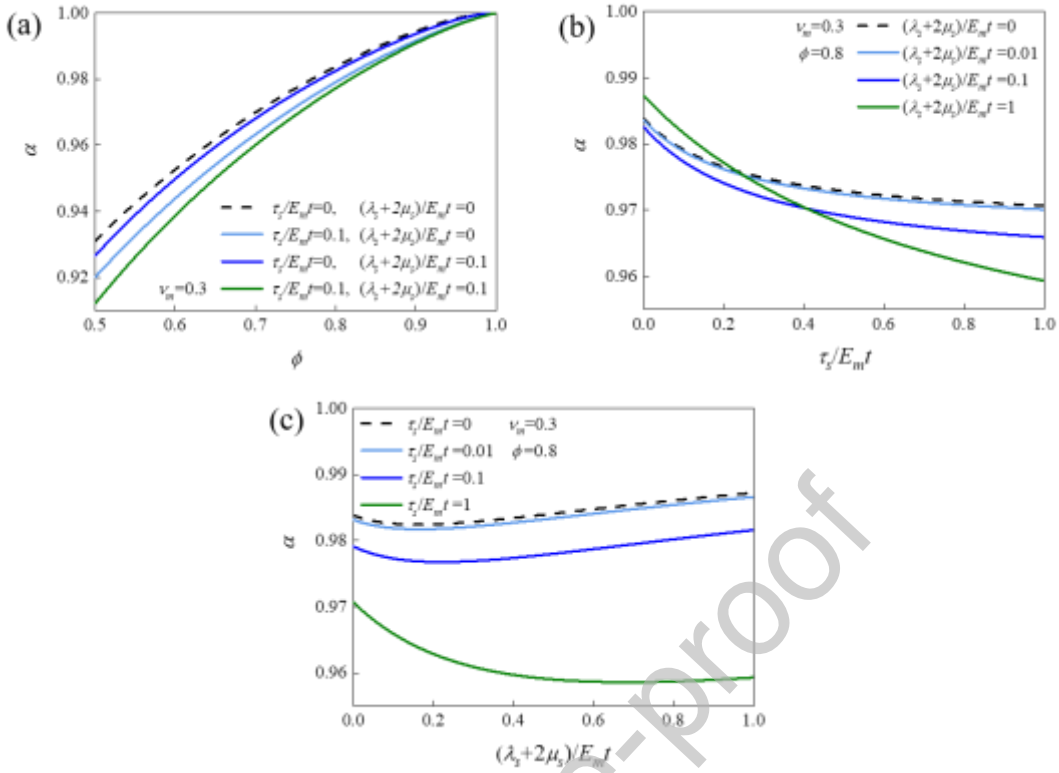

Figure 7. Dependence of Biot coefficient of effective stress on porosity and surface effects. (a) Influence of porosity, with the Biot coefficient increases with increasing porosity. (b) Influence of residual surface stress, with the Biot coefficient decreases with the increase of residual surface stress. (c) Influence of surface moduli, with the Biot coefficient decreasing first and then increasing as surface moduli are increased. For the plotting, $\nu_m = 0.3$ and $\phi = 0.8$ are selected.

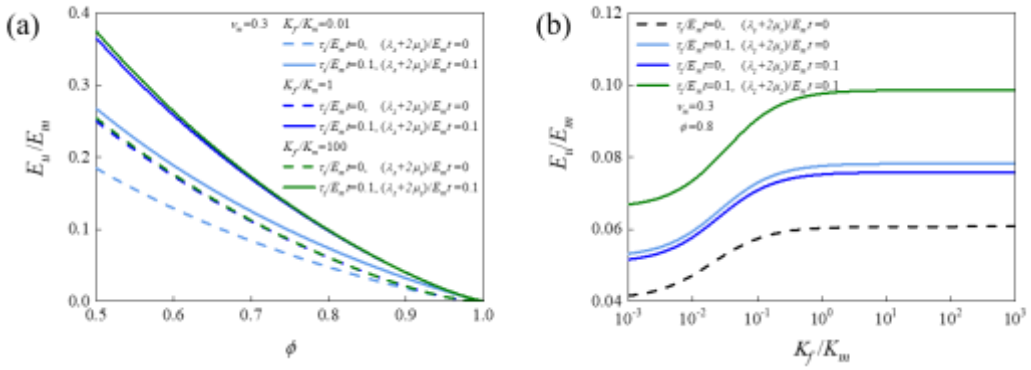

Figure 8. Influence of porosity and fluid bulk moduli on effective undrained Young's modulus. (a) Effective undrained Young's modulus decreases with increasing porosity ($\nu_m = 0.3$ and $K_f/K_m = 0.1$). (b) Effective undrained Young's modulus increases with the increase of fluid bulk modulus ($\nu_m = 0.3$ and $\phi = 0.8$).

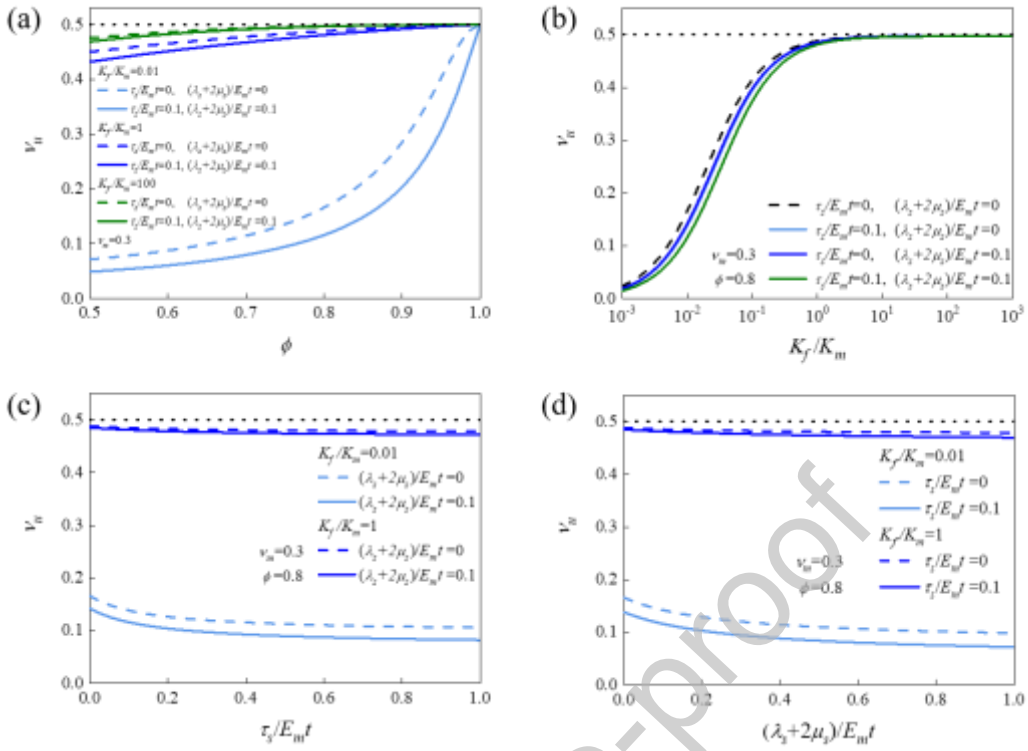

Figure 9. Influence of porosity, fluid bulk modulus and surface parameters on effective undrained Poisson ratio. (a) Influence of porosity, with the effective undrained Poisson ratio increasing with the increase of porosity. (b) Influence of fluid compressibility, with the effective undrained Poisson ratio increasing with the increase of fluid bulk modulus. (c) Influence of residual surface stress, with the effective undrained Poisson ratio decreasing with the increase of residual surface stress. (d) Influence of surface moduli, with the effective undrained Poisson ratio decreasing with the increase of surface moduli. For the plotting, $\nu_m = 0.3$ and $\phi = 0.8$ are selected.

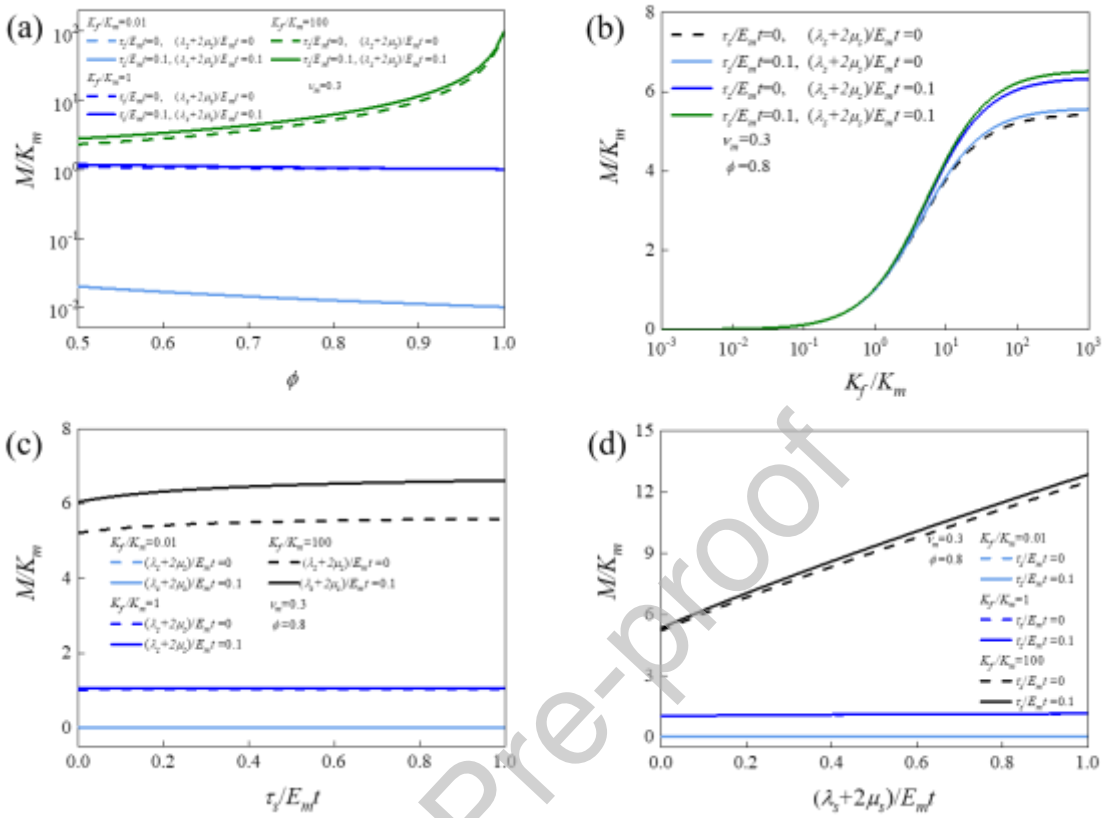

Figure 10. Dependence of effective Biot modulus on porosity, fluid compressibility and surface stress. (a) Influence of porosity, with the effective Biot modulus decreasing for small fluid bulk modulus and increasing for large fluid bulk modulus as porosity is increased. (b) Influence of fluid compressibility, with the effective Biot modulus increasing with increasing fluid bulk modulus. (c) Influence of residual surface stress, with the effective Biot modulus increasing with the increase of residual surface stress. (d) Influence of surface moduli, with the effective Biot modulus increasing with increasing surface moduli. For the plotting, $\nu_m = 0.3$ and $\phi = 0.8$ are selected.

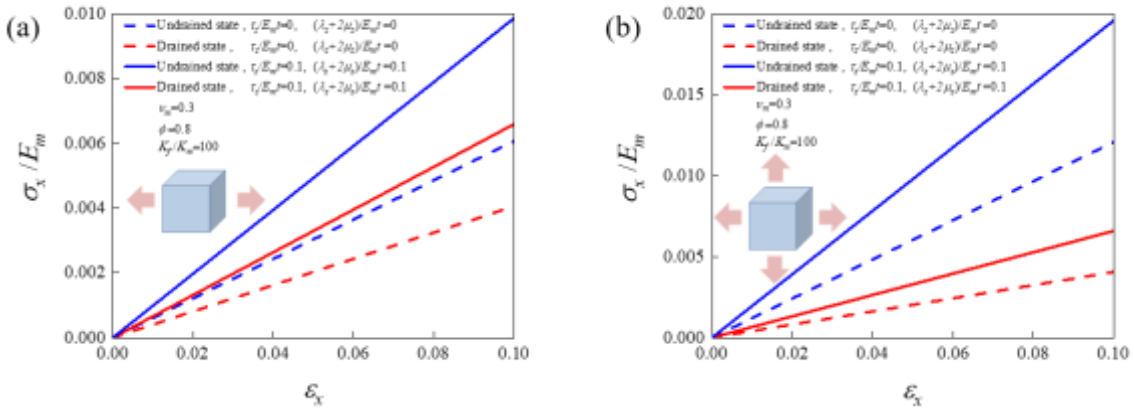

Figure 11. Stress versus strain curves under (a) uniaxial tension and (b) non-proportional tension for porous materials under either undrained or drained state.

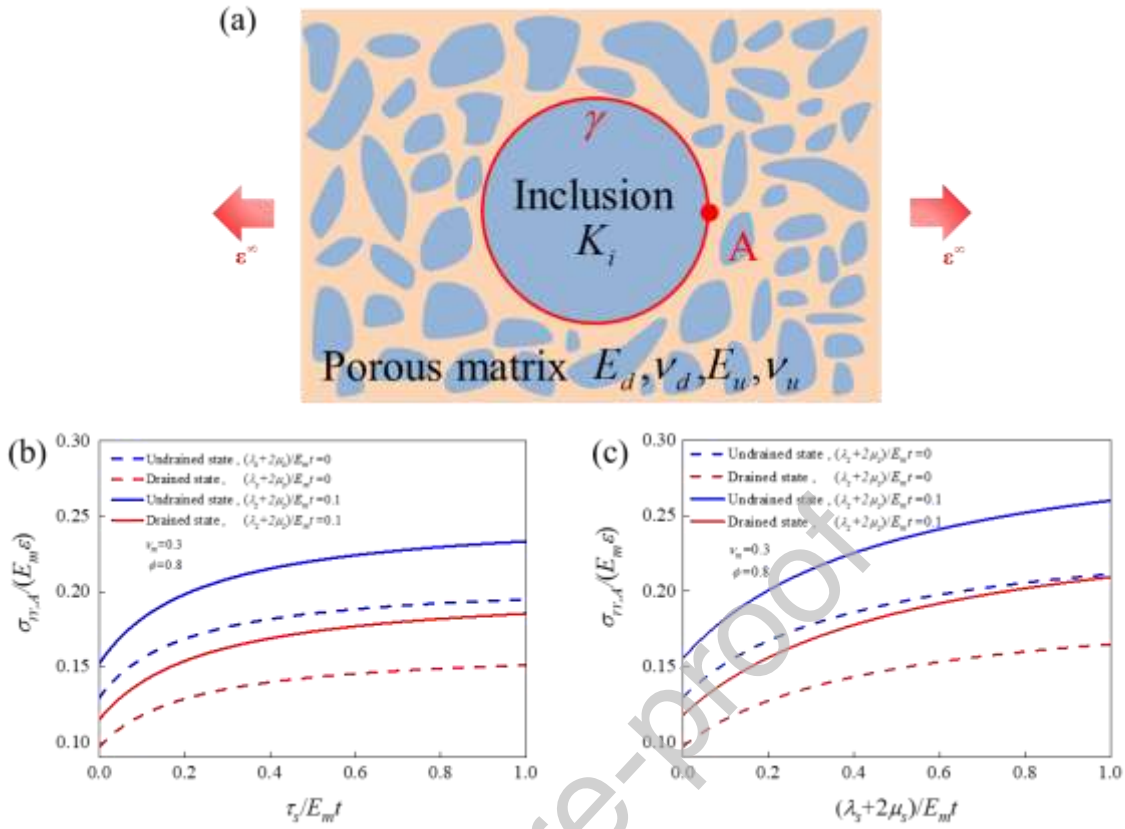

Figure 12. Dependence of radial stress of spherical liquid inclusion in fluid-saturated porous matrix on surface effects. (a) Schematic of a spherical liquid inclusion surrounded by an infinite saturated poroelastic matrix with double influence of surface effects surface effects, subjected to uniaxial stretching at remote. Surface tension on inclusion-matrix interface is denoted by γ. (b) Influence of residual surface stress on radial stress σ_{rr} at point A, with different line styles representing different states and different colors representing different surface moduli. The radial stress increases with increasing residual surface stress. (c) Influence of surface moduli on radial stress σ_{rr} at point A, with different line styles representing different states and different colors representing different residual surface stress. The radial stress increases with increasing surface moduli. For the plotting, $\nu_m = 0.3$, $\phi = 0.8$, $K_i = 0.1K_m$ and $\gamma = 0.1E_m R$ are selected.

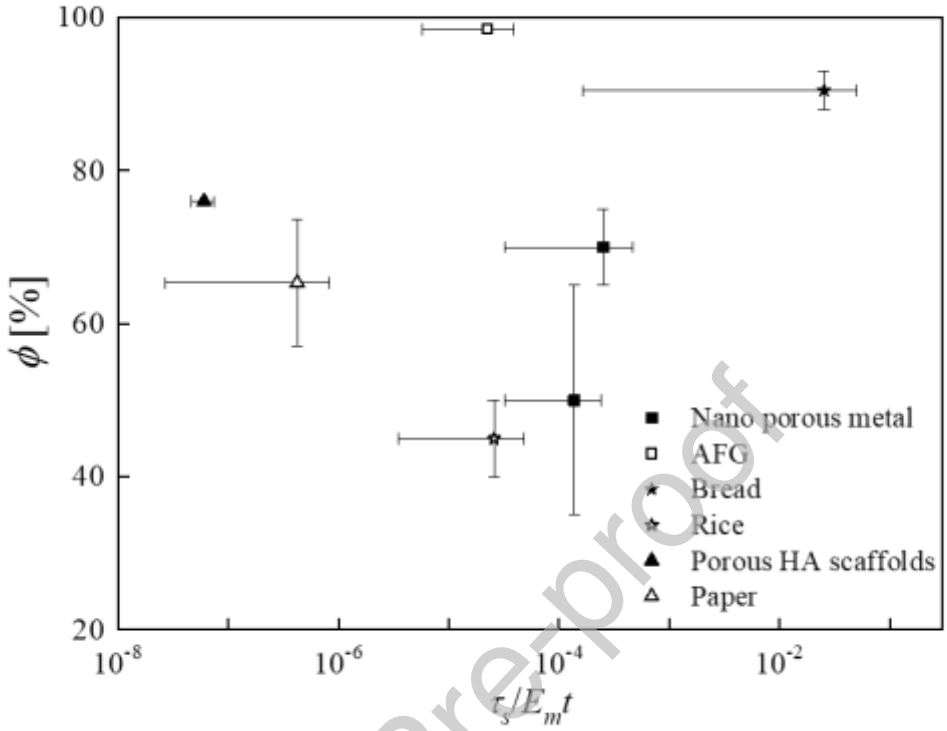

Figure 13. Residual surface stresses and porosities of common fluid-saturated porous materials.